The role of fluoride and fluorocarbons in enhanced stability and performance of halide perovskites for photovoltaics

Benjamin M. Lefler, Steven J. May, and Aaron T. Fafarman^{2,*}

¹ Department of Materials Science and Engineering, Drexel University, Philadelphia, Pennsylvania 19104, USA

² Department of Chemical and Biological Engineering, Drexel University, Philadelphia, Pennsylvania 19104, USA

Corresponding Author: fafarman@drexel.edu

Abstract:

Halide perovskites are promising absorber materials for photovoltaics due to their high efficiency and low-temperature solution processing, though the instabilities inherent to these systems remain a primary obstacle to their utilization. In this Research Update, we review the chemical, structural, and functional effects of fluoride and fluorinated organic additives in halide perovskites, especially on stability and photovoltaic performance. We detail the evidence that, when incorporated as its anion, fluoride is typically localized to perovskite surfaces and grain boundaries. Due to its high electronegativity, fluoride and fluorinated species can impart strong ionic and intermolecular bonding with perovskite materials, passivating surfaces and diminishing their susceptibility to further chemical reactivity. Additionally, fluorocarbon-based additives impart hydrophobicity to perovskite films and serve as physiochemical barriers to reactive infiltrating species. To understand how these effects operate in different contexts, herein we summarize the dual role surface defects play in both diminishing photovoltaic efficiency and introducing structural instabilities in various ABX₃ perovskite halide materials: hybrid organic/inorganic lead halide, all-inorganic cesium lead halide, and tin halide perovskites. We review three avenues of fluorine inclusion in perovskites: fluoride substitution at the anion site, partial incorporation of fluorinated organic cations at the A-site, and large- and smallmolecule fluorocarbon-based additives. We conclude with a perspective on the prospects for fluorinebased enhancement of halide perovskites and suggestions for new analytical and synthetic chemistries that will deepen our understanding and control of these systems.

I. INTRODUCTION

Organolead trihalide perovskites and their derivatives have been at the forefront of photovoltaic materials research since their initial demonstration in 2009 by Kojima *et al.* with a simple solar cell working at 3.8% power conversion efficiency (PCE) [1]. In the span of a decade, efficiencies of perovskite solar cells have soared at a rate unprecedented in the photovoltaic (PV) field to 25.2% [2], becoming competitive with silicon-based technologies. Typical halide perovskites follow the traditional perovskite ABX_3 chemical formula, commonly with an organic cation such as methylammonium (MA⁺, CH₃NH₃⁺) in the *A* site, a heavy post-transition metal such as Pb²⁺ in the *B* site, and a halide such as I⁻ in the *X* site. However, many permutations of perovskite phases have been explored through substitution in each of the sites by alternative ions.

The excitement propelling this family of materials is multifaceted. From a materials physics perspective, the halide perovskites excel as PV absorbers due to their high absorption coefficients, direct band-gaps within the optimal range for PV applications, low exciton binding energies, and long carrier diffusion lengths and lifetimes stemming from unusual recombination physics and inherent defect tolerance [3–5]. From a processing perspective, defect tolerance enables devices to be fabricated through low-temperature, low-cost, and low-complexity solution processes, highlighting the enormous scaling potential for perovskite solar cells [6]. However, one of the major obstacles inhibiting commercial cells is the innate instabilities found in the various flavors of the halide perovskites. While discussed in-depth in the next section, these modes of instability include degradation of MAPbl₃ to Pbl₂ through phase separation and sublimation of MAI, phase transformation from photoactive cubic (or pseudo-cubic) $APbl_3$ ($A = Cs^+$, $CH(NH_2)_2^+$) perovskite phases to inactive orthorhombic ($A = Cs^+$) and

hexagonal (*A* = CH(NH₂)₂⁺) phases, and tin oxidation in *A*SnI₃. While the mechanisms differ, two of the common catalysts of instability are infiltrating water and oxygen molecules; for both species the barrier to infiltration is lowered by the presence of surface defects. Prior to causing material degradation, surface defects are also sources of diminished PV performance. For instance, surface/interface-specific defects can introduce deep level trap states that are sites of non-radiative recombination, hydration of MAPbI₃ bleaches its photoabsorption spectrum, and oxygen can intercept charge carriers through parasitic reduction to superoxide. With surface states serving as mechanistic sources of both diminished performance and decreased stability in perovskite halide photovoltaics, routes to mitigate one issue conveniently benefit the other as well.

In this Research Update, we first present the argument given in the literature that many of the instability and inefficiency issues in halide perovskite photovoltaics stem from surface defect states which themselves stem from the shallow potential energy landscape that separates functional (perovskite) and non-functional phases. As an illustrative example, the formation enthalpy of MAPbl₃ relative to solid precursors MAI and Pbl₂ has been found to be on the order of thermal energy at room temperature, $N_A k_B T = 2.5 \text{ kJ/mol } [7-9]$. At surfaces and grain boundaries, this manifests as readily formed defects with high mobility [10,11], leaving the material susceptible to surface-specific trap states and degradation catalyzed by water and oxygen. We describe the benefit of fluorine-based routes to strengthen the bonding architecture at surfaces and grain boundaries as well as prevent the encroachment of detrimental species. Specifically, fluorine, owing to its small size and large electronegativity, can improve the ionic bonding compared to that between the perovskite *B*-site cation and the other halides, and its electron withdrawing nature can increase dipole moments in the perovskite to improve the intermolecular bonding between the organic cation and BX_6 octahedral framework. Generally speaking, fluorine makes for exceedingly strong ionic bonding (i.e., ΔH_f of Pb-F = 356 kJ/mol vs. Pb-I = 197 kJ/mol in PbX₂ [12]). Similarly, metal fluorides are capable of forming strong

hydrogen bonds, with ΔH_f for M—F---H—N bond as low as -20 kJ/mol [13], which are much stronger than hydrogen bonds formed by metal iodides [14,15]. Additionally, fluorocarbons are known to exhibit hydrophobicity and can therefore provide further protection against infiltrating species.

The remainder of this Research Update will highlight three overarching motifs in stabilization and PV enhancement of ABX_3 halide perovskites with fluorine, shown in Figure 1: fluoride anions incorporated into the X-site (shown in Figure 1a), partial incorporation of fluorinated cations at the A-site (including in mixed-dimensional perovskites, shown in Figure 1b), and fluorocarbon-based additives as secondary phases, i.e., multilayers and composites (shown in Figure 1c).

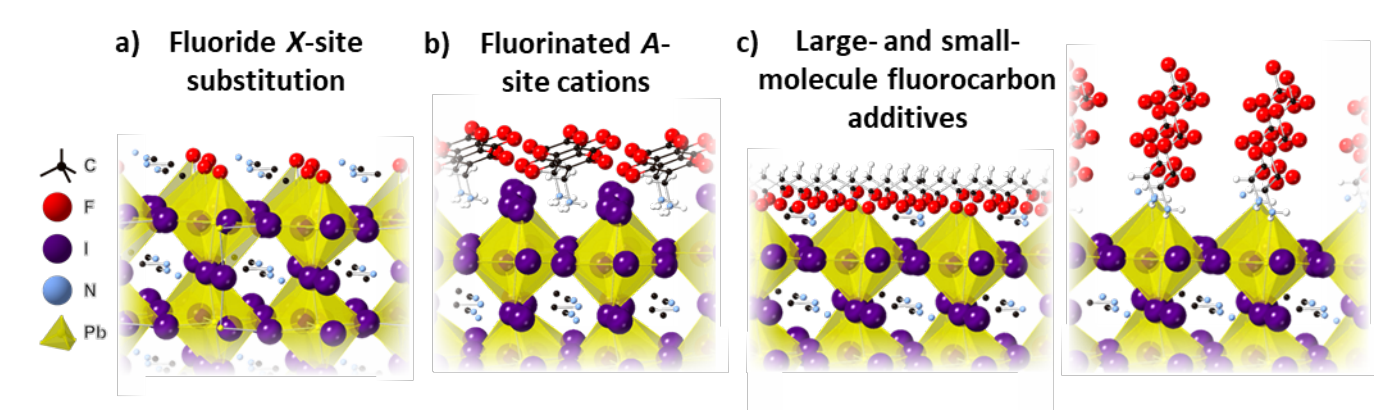


FIG. 1. Approaches to improve perovskite PV performance and stability through passivation with fluorine-containing agents. a) Terminal X-site substitution with F^- . b) Fluorinated organic cations to occupy terminal A-sites (shown: C_6F_5 - CH_2 - NH_3 +). c) Fluorocarbon-based additives such as fluoropolymers (left, shown: polyvinylidene fluoride) and small-molecules (right, shown: 1H,1H-perfluorohexyl amine) to coordinate perovskite surfaces. Crystal structure for MAPbI₃ was rendered from crystallographic data found in reference [16].

While the field of halide perovskite optoelectronics is quite expansive, this Research Update will focus only on the benefits of incorporating fluorinated moieties into thin film photovoltaics. The inclusion of extrinsic species (e.g. dopants and surfactants) can have various secondary or non-specific effects such as improved crystal morphology, however this Research Update is particularly interested with the direct changes in bonding and hydrophobicity and hence function imparted by fluorine-containing species. Perovskite quantum dot technologies and perovskite light-emitting diodes have been reviewed elsewhere and will not be discussed [17–19].

II. PV PERFORMANCE LIMITATIONS AND DEGREDATION MECHANISMS IN PEROVSKITE DERIVATIVES

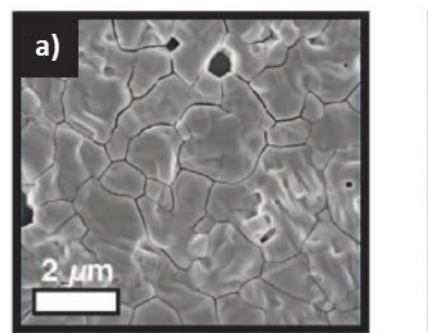
The scope of this Research Update encompasses three halide perovskite materials systems, though the majority of current literature focuses on one system in particular, MAPbl₃. Therefore, the current understanding of PV-limiting electronic defects discussed in section II-A is based in studies of the prototypical MAPbl₃. However, these concepts should be applicable to all halide perovskite systems. On the other hand, each of the three systems discussed herein suffers from unique chemical and structural instabilities. In sections II-B,C,D, we will provide a brief overview of the mechanisms behind each system's instability.

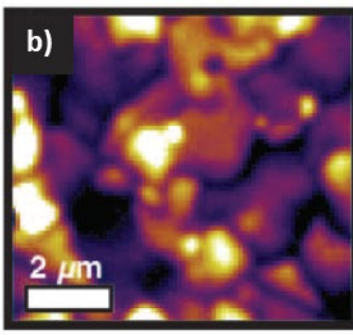
A. The role of surface defects in diminished PV performance in halide perovskites

As introduced above, perovskite halides are ideal PV absorber materials in regard to photoabsorption and carrier kinetics. However, due to relatively low defect-formation energies [20], they also readily support point defects such as vacancies, interstitials, and antisite substitutions. While perovskite halides are widely lauded to be defect-tolerant materials, reduced photoluminescent (PL) response has been observed at surfaces and grain boundaries (GBs), as shown in Figure 2 through SEM (Figure 2a) and fluorescent (Figure 2b) imaging and their corresponding overlay (Figure 2c), experimentally indicating some source of deep trap-facilitated non-radiative recombination [21].

Theory tells us that point defects in perovskite halides contribute only benign states within the bands or shallow trap states as in the cases of I⁻ interstitials (I_i) and I⁻ vacancies (V_i) (Figure 3a), or otherwise have prohibitively high formation energies as in the case of Pb²⁺ interstitials (Pb_i, 1.85-4.24 eV) (Figure 3a,c) [20]. Therefore, to understand how such "defect-tolerant" materials nonetheless can exhibit problematic defects, it is necessary to focus on surficial and interfacial defects. For example, Kong *et al.* [22] attributed deep trap surface states in MAPbI₃ to iodide-rich environments vs. iodide-

poor environments at surfaces. The authors deposited films with controlled surface environments (I-rich and I-poor) and experimentally showed a stark contrast in PL characteristics between the two. Films with I-poor surfaces displaying longer average carrier lifetimes of 66.5 ns and monomolecular decay, while I-rich surface films displayed shorter average lifetimes of 18.2 ns and bimolecular PL decay.





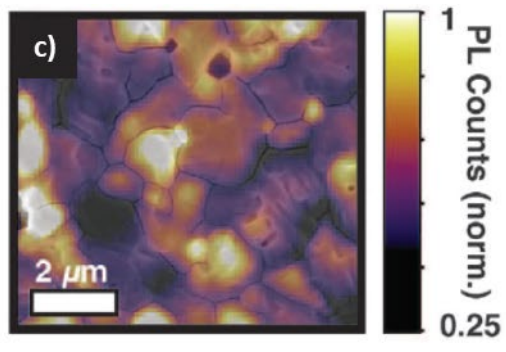


FIG. 2. A comparison of (a) an SEM image and (b) fluorescent microscopy of spatial variation in photoluminescence of the same area of a MAPbl₃(Cl) film; (a) and (b) are overlaid in (c), showing a correlation between grain boundaries and diminished PL intensity. Reprinted from reference [21], with permission. Copyright 2015, American Association for the Advancement of Science.

Uratani *et al.* [23] contributed further to our understanding of perovskite halide surface defect states with a first-principles study comparing the energy levels (Figure 3b) and formation energies (Figure 3c) of possible surface defects of various termination motifs: MAI-terminated, PbI₂-terminated (Figure 3b top), and PbI₂-terminated with vacancies of PbI₂ units (PbI₂/vacant, Figure 3b bottom), each with specific possible environments: I-rich, Pb-rich (I-poor), and intermediate conditions. They concluded that MAI-terminated surfaces do not contribute to deep-level trap states - though we note that considering the volatility of MAI, it is not expected that these termination scenarios are present experimentally. On the other hand, the authors reported that PbI₂-terminated surfaces support low formation energy I₁ (-0.03 eV) defects in I-rich environments, and PbI₂/vacant-terminated surfaces support I₁ (-0.12 eV) and Pb₁ (0.26 eV) defects in I-rich and Pb-rich environments, respectively (Figure 3c). Figure 3a,b shows the calculated energy levels of a subset of possible defects, and Figure 3c gives a full summary of formation energies of these defects for all of the discussed conditions; the formation energies of problematic

deep-level energy states are bolded. The subset of bolded (deep-level) defects that exhibit low formation energy are the states predicted to be most responsible for surface-associated recombination. Kim and Lee [24] elucidated further surface defect mechanisms in terms of charge localization, concluding from first-principles calculations that localized charges stabilize the formation of lead dimers and I-V_I-I trimers which serve as long-term trap states for charge carriers. In summary, grain boundary/surface states in halide perovskites support unique defect motifs that do contribute to deep-gap states and subsequent nonradiative recombination and diminished PCE, in contrast to the "defect tolerant" behavior of the bulk interior, wherein such point defects either have prohibitive formation energies or do not exhibit deeply mid-gap energies.

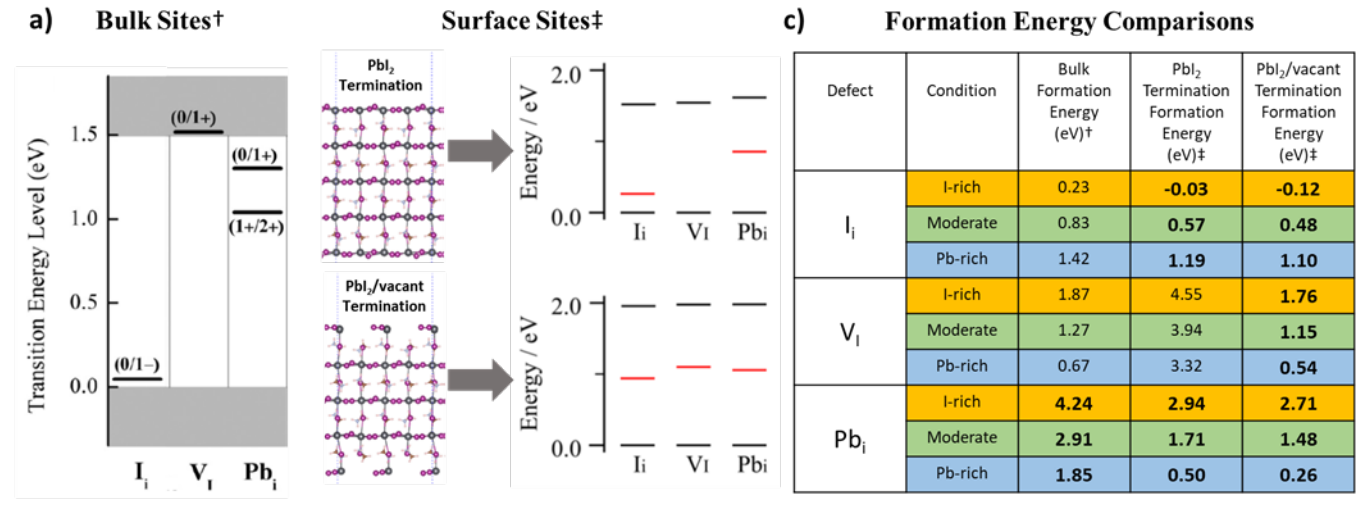


FIG. 3. a) Bulk site defect energy levels in MAPbI₃ with associated defect charges. b) Surface site defect energy levels for PbI₂ flat-terminated surfaces (top) and PbI₂/vacant-terminated surfaces (bottom) with associated models. c) Formation energies for each defect in I-rich, Pb-rich, and intermediate local chemical conditions, for each defect location (bulk, PbI₂-terminated, and PbI₂/vacant-terminated). Formation energies for defect sites and conditions associated with deep trap states are bolded. The figure and data for bulk sites† are adapted from reference [20], with permission. Copyright 2014, AIP Publishing. The figures and data for surface sites‡ are adapted from reference [23], with permission. Copyright 2017, American Chemical Society. Further permissions related to this content should be directed to the ACS.

It follows that various treatments of surface coordination and termination chemistries have been shown to passivate these surface defect states and enhance PV performance. Some examples of passivating ligands include nucleophilic small molecules [21,25], A-site cationic anchors [26],

supramolecular halogen bonding small molecules [27,28], oxysalts [29], and coordinating polymers [22], though there have been many more in the literature. A full review of the demonstrated passivation techniques in the literature is well beyond the scope of this article, but we recommend further reading in references [30–32].

B. MAPbl₃ degradation to Pbl₂

Surface vacancy sites, in addition to the direct electronic effects detailed above, also serve as points of exploitation by infiltrating species like water and oxygen. These species, aided by ultraviolet (UV) light, accelerate MAPbl₃ degradation through phase separation of Pbl₂ and volatilization of MAI. Though MAI can sublimate without the presence of moisture, it has been reported experimentally [33,34] and through calculations [35-37] that water molecules lower the formation energy of halide vacancy surface defects through MAI solvation at grain boundaries, promoting water penetration through solvation of vacancy-riddled Pbl₂-terminated perovskite surfaces. Water has been proposed to act as a Lewis base, deprotonating MA⁺, thus lowering the barrier to volatilization of CH₃NH₂, and in the process releasing HI, regenerating water, and leaving behind solid Pbl₂ [38]. Since it is not consumed in this cycle, even trace amounts of water can catalyze ongoing degradation. Additionally, it has been shown that under no illumination, humidity causes the formation of a surface-initiated dihydrate, (CH₃NH₃)₄PbI₆·2H₂O, which effectively bleaches the material's photoabsorption spectrum; upon illumination, the dihydrate undergoes especially facile degradation to Pbl₂ [39]. For oxygen's role, it has been reported that molecular oxygen accepts photoexcited free electrons from the perovskite and reduces to superoxide (O_2^-) [40]. UV light enhances the bulk penetration by molecular oxygen via iodide vacancy pathways and activates superoxide to deprotonate the MA⁺, ultimately producing methylamine, water, I₂, and Pbl₂ [40–44]. UV light also induces perovskite degradation in perovskite solar cells that contain TiO₂ – a commonly used electron transport material (ETM) - through surface catalytic activation at the

perovskite-TiO₂ interface [45]. The degradation described herein was theoretically and experimentally reported to proceed as a layer-by-layer process initiated at surfaces and grain boundaries where the material is susceptible to water and oxygen attack and where the energetic barrier to phase separation is smallest [46,47]. The degradation can be clearly seen as a conversion of the black MAPbl₃ film to yellow Pbl₂, shown in Figure 4. In-depth discussions of these degradation mechanisms are beyond the scope of this article but are easily accessible in various review articles [43,48–53].

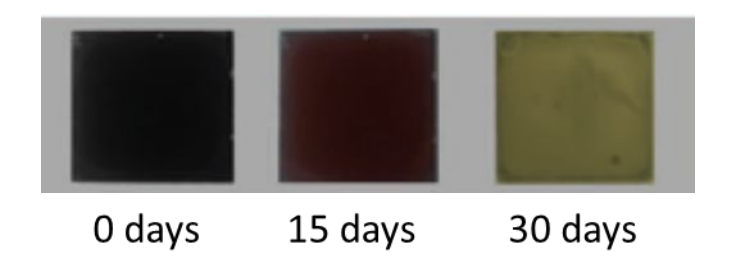


FIG. 4. Degradation of MAPbl₃ film (left, black) to Pbl₂ (right, yellow) over 30 days stored in air at 50% RH. Reprinted from reference [54], with permission. Copyright 2019, John Wiley and Sons.

C. CsPbl₃ and FAPbl₃ phase instability between photoactive black and inactive yellow phases

There are two alternative A-site cations that ameliorate the problem of volatility posed by methylammonium: formamidinium (CH(NH₂)₂+, FA+), and to an even greater extent, cesium. FAPbI₃ exhibits a band gap even closer to the ideal value for single-junction solar cells, while CsPbI₃ offers the attraction of being an all-inorganic alternative. However, despite both alternative perovskites possessing greater stability toward phase separation and volatilization, both suffer from a different instability: a structural instability of the perovskite phase.

A simple yet useful empirical indicator of the equilibrium phase stability of perovskite materials is the Goldschmidt tolerance factor [55], which is a numerical comparison of the relative ionic sizes of A, B, and X. Traditionally, materials with a tolerance factor between 0.8 and 1.0 tend toward stable perovskites. Cs $^+$ is a smaller ion than MA $^+$ (with respective ionic radii of 167 pm and 217 pm), resulting in

a Goldschmidt tolerance factor of 0.81 for CsPbI₃, at the border of perovskite stability [56]. Instead, CsPbI₃ crystallizes into an equilibrium yellow (PV-inactive), orthorhombic δ -phase at room temperature. The desired black (PV-active) perovskite α -phase is stable at temperatures greater than ~320 °C and can be obtained at room temperature by thermal quenching to kinetically trap the black phase. However, upon exposure to air, there is a reversion on the order of minutes from black to yellow phase in the perovskite at room temperature [57,58]. It has been reported that this reversion is slowed by orders of magnitude in inert environments, and indications point to water as the environmental catalyst that begins the phase transformation back to the yellow phase. As such, a surface coordination/passivation approach has been shown to help prevent catalysis and stabilize the black phase [59].

On the other end of the spectrum, FA⁺ is a larger ion than MA⁺ (with ionic radii of 253 pm and 217 pm, respectively), and the resulting Goldschmidt tolerance factor for FAPbI₃ is calculated to be 0.99, which borders the upper limit for a stable perovskite structure [56]. Therefore, the metastable, photoactive, cubic α-phase FAPbI₃ reverts to an inactive, yellow, hexagonal δ-phase at room temperature. Much like the case of CsPbI₃, the cubic phase of FAPbI₃ can be kinetically trapped at room temperature and be maintained until reversion to the inactive phase is catalyzed by moisture [60] which notably initiates at surfaces and grain boundaries [61,62].

D. ASnI₃ degradation by Sn²⁺ oxidation to Sn⁴⁺

While the lead halide perovskites are a fantastic material system for reasons previously discussed, there is also an ecological push to move away from lead-based systems. Tin substitution has been proffered as a viable substitution for lead, as Sn is found directly above Pb on the periodic table. However, the tin halide perovskites suffer from yet other unique instabilities. Unlike in the lead-based perovskites, density functional theory (DFT) calculations purport that the most energetically favorable point defect in this system is the *B*-site (Sn) vacancy, which leads to *p*-type doping of the material and is

often seen experimentally [63,64]. Therefore, excess tin sources are often employed to reduce the number of these vacancies [65]. However, also unlike Pb^{2+} , Sn^{2+} has the tendency to oxidize to Sn^{4+} , so in the presence of oxygen, the tin halide perovskites have been shown to degrade to SnO_2 and another Sn(IV) phase, notably A_2SnX_6 [66,67]. In this case, oxygen is a more favorable competitor than the halide to chemically bond with tin at the surface at equilibrium. A more in-depth review of tin halide instabilities can be found in reference [68].

E. Instability commonalities and the role of fluorine in improvement of stability and PV performance

Though each perovskite system reviewed in this section – hybrid organic-inorganic MAPbl₃, stretched-tolerance factor CsPbl₃ and FAPbl₃, and lead-free CsSnl₃ – suffers from instability issues that are specific to its respective composition, we can find a commonality in addressing the causes of these instabilities as well as PV underperformance. At the risk of oversimplification, the mechanisms illustrate that relatively weak bonding in the perovskite allows for ion migration and surface/GB defect formation, and reactive, infiltrating species such as water and oxygen exploit these surface/GB defects to catalyze phase separation or transformation. In addition, it has repeatedly been experimentally demonstrated in halide perovskite research that passivating surfaces and interfaces to general defects and trap states mitigates recombination, despite the materials exhibiting defect tolerance in bulk [21,25,26,30,69–71]. It follows that the routes to stabilization and PCE improvement in any of the perovskite systems discussed above may involve: 1) The formation of strongly bonded adducts to terminate surfaces and grain boundaries that do not introduce mid-gap states (e.g., electronic defect passivation); 2) Occupying the docking sites at surfaces and interfaces that harmful infiltrating species like water and oxygen require; 3) Preventing diffusion of parasitic species like water and oxygen from perovskite surfaces into the bulk. These goals lend themselves particularly to the innate qualities of fluorine and various fluorocarbons, including the typical strong and highly stable bonding and coordination chemistries associated with fluorine compounds and the well-established hydrophobicity of fluorocarbons.

III. FLUORIDE X-SITE ANION SUBSTITUTION IN PEROVSKITES

Having established in section II that PV efficiency and stability deficiencies in halide perovskites can generally be attributed to surface defects due to weak bonding, the advantages of strengthening bonding at the surfaces through substitution become evident. There has been considerable work in alloying lead iodobromide perovskites for improved stability through the shrinking and strengthening of Pb-X bonds with increasing bromine content [72,73]. However, this is accompanied by an increasing of the band gap, moving away from ideality for a single-junction solar cell, as well as a new, functional instability of photoinduced de-alloying [74,75]. If we continue to march up the periodic table to exploit stronger bonding with smaller ions, we come to chlorine. Chloride salts have been used in halide perovskite deposition with promising improvements in PV performance [21,76] and stability [77]. However, unlike with bromide alloying, iodochloride perovskites show no difference in structure (X-ray diffraction, XRD) nor photoabsorption (UV-vis spectroscopy) from the pure iodide. It is therefore concluded that chloride is not incorporated into the bulk perovskite lattice due to the prohibitive ionic size difference (i.e., APbCl₃ and APbl₃ do not form solid solutions; r_{Cl}. = 181 pm, r_l. = 220 pm [78]). Instead, chloride has been reported to enhance crystallization kinetics to improve morphology [79–81]. Interestingly, de Quillettes et al. also revealed through fluorescent microscopy and energy dispersive xray spectroscopy (EDS) that a presence of Cl⁻ (up to ~2%) is coincident with MAPbl₃(Cl) grains with brighter photoluminescence [21] as seen in Figure 5. Therefore, it is possible that the chloride ions in their study were excluded from grains but acted as strongly-bonding surface ligands to heal trap states. We posit that a similar phenomenon of localization likely occurs when fluoride, rather than chloride, is the impurity. In this section, we will review the potential use of fluoride anions as surface ligands for halide perovskites. By strongly coordinating surface lead ions, fluoride can occupy surface vacancies, remove mid-gap electronic states, and stabilize exposed surfaces against water or oxygen attack.

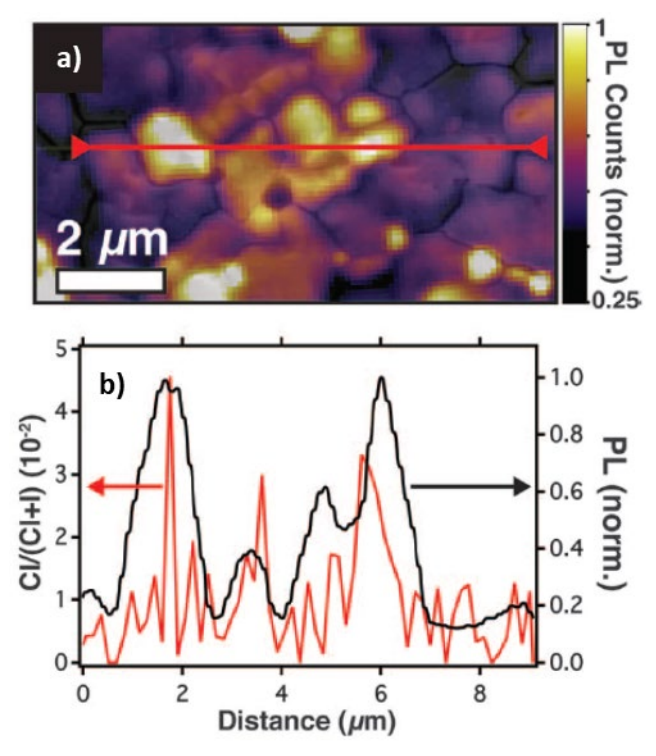


FIG. 5. a) Overlay of SEM and fluorescent imaging of a MAPbl₃(Cl) film. b) A line scan (shown in part (a)) of PL intensity and corresponding chloride response measured by EDS, showing a correlation between chloride concentration and increased PL intensity. Reproduced from reference [21], with permission. Copyright 2015, American Association for the Advancement of Science.

A. Fluoride treatment of tin halide perovskites to mitigate Sn oxidation

Fluoride salts were first and most prominently used in perovskite halides in the lead-free tin halide perovskites, $ASnX_3$. The first report was in 2012 by Chung *et al.* [82] where $CsSnI_3$ was being used as a hole-transport material in a dye-sensitized solar cell. By treating the perovskite with 5 mol % SnF_2 , they reported increases in cell performance by enhancing open circuit voltage (V_{OC}) and short circuit current (V_{OC}). Addition of SnF_2 (in optimized ratios) has been shown to reduce trap states using time-resolved PL (TRPL) [83], time-resolved surface photovoltage measurements [84], Hall measurements [85], capacitance-voltage profiling [86], and electrical impedance spectroscopy (EIS) [87]. As with the chlorides in lead perovskites [88,89], the fluoride in this system is not incorporated into the perovskite, as evidenced by a lack of peak shift in XRD [86,87], presumably due to ion size mismatch,

though it is dispersed throughout the perovskite layer according to X-ray photoelectron spectroscopy (XPS) experiments [85]. It is therefore reasonable to expect the fluoride to inhabit perovskite grain boundaries and surface sites.

As discussed in section II-D, tin halide perovskites suffer PV inefficiencies caused by Sn vacancies, so the trap filling is mainly attributed to the addition of excess Sn, and indeed this trap healing can be provided by fluoride-free Sn salts as well [68]. However, the incorporation of fluoride additionally improves the stability of tin halide perovskites [90,91]. When exposed to air, ASnX₃ can decompose to A₂SnX₆ on the order of hours to days, driven by Sn oxidation to SnO₂ by atmospheric oxygen. Wu et al. [92] showed that with systematic fluoride doping, this transition can be slowed considerably. The authors monitored phase changes in films of CsSnI₃ with different extents of fluoride doping, which goes first through a phase change between black (B-CsSnI₃) and yellow (Y-CsSnI₃) polymorphs of CsSnI₃ before finally degrading to black Cs₂SnI₆ due to Sn oxidation. Visually, they showed that while undoped B-CsSnI₃ films converted to Y-CsSnI₃ within an hour of air exposure and to Cs₂SnI₆ within 6 hours, moderately F-doped films ($F^- = 3.7-7.3\%$ of total X^-) took 6 and 24 hours, respectively, to make the two transitions, and highly F-doped films (F⁻ = 11%) still exhibited Y-CsSnI₃ peaks in XRD even after 7 days of air exposure. Zhao et al. [93] used DFT calculations to investigate the impact of Fincorporation on the local bonding architecture of the perovskite structure (Figure 6). They concluded that fluoride in this system strongly localizes electron density from the Sn 5p highest occupied molecular orbital (HOMO) tightly to the Sn atom, as seen in the electron density mapping of the undoped vs. Fdoped perovskite unit cells shown in Figure 6a and 6b, respectively, and this strong localization inhibits Sn oxidation, i.e., that which results in molecular oxygen reduction at the perovskite surfaces.

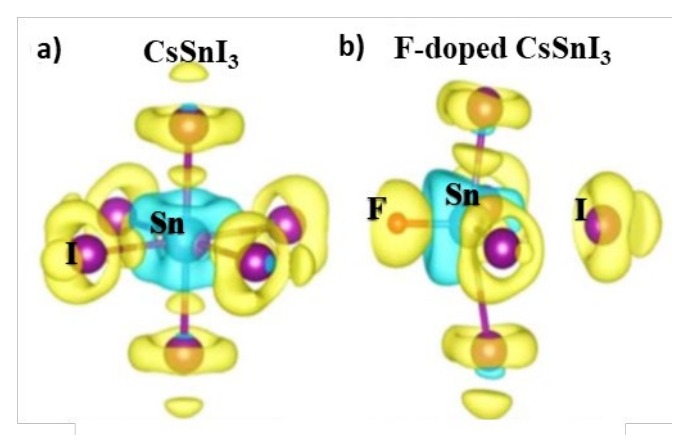


FIG. 6. Calculated charge density differences for (a) pristine CsSnI₃ and (b) F-doped CsSnI₃. Yellow and blue regions are electron accumulation and depletion zones, respectively. Reprinted from reference [93], with permission. Copyright 2019, IOP Publishing Ltd.

In practice, it should be noted, SnX_2 supplementation has a non-specific effect on film morphologies due to the limited solubility of SnX_2 salts and their tendency to self-aggregate. It is reported that small doses improve uniformity by increasing the number of nucleation sites during crystallization [87]. However, larger doses can have the opposite effect, resulting in rough films with voids and pinholes due to aggregation. This aggregation can be mitigated by using a Lewis base additive to coordinate SnX_2 and improve solubility [94].

Though the remainder of this Research Update discusses the more ubiquitous lead halide systems, the tin halides provided the earliest precedent for capitalizing on the tight binding of fluoride to stabilize surfaces of halide perovskites.

B. Fluoride treatment of lead iodide perovskites

Fluoride doping in lead iodide perovskites was, to our knowledge, unexplored until 2019. Li *et al.* [95] broke ground in this area by dissolving 0.1% NaX ($X = I^-$, Br $^-$, Cl $^-$, F $^-$) salts in triple cation (mixed Cs/MA/FA) perovskite precursor solutions prior to deposition. For discussion, the authors refer to the control films as CsFAMA, and each of the doped films as CsFAMA-I, CsFAMA-Br, CsFAMA-Cl, and CsFAMA-F. Scanning electron microscopy (SEM) images revealed that while I- and Br- doping had no

effect on the morphology of the perovskite films, CI-doping produced films with larger grains as expected from previous reports [76,80], while F-doping had a similar but even more pronounced effect, indicating a similar role in crystallization kinetics that chloride is known to assume. On an atomic scale, F-doping also appears to be akin to Cl-doping in that F was not incorporated into the perovskite bulk, as evidenced by no change in the optical absorption/emission spectra nor in the XRD pattern relative to the control films. However, interactions between F and the perovskite were observed using infrared (IR) spectroscopy in which the N-H stretch of the organic cation was weakened (Figure 7a), indicating hydrogen bonding to F⁻, and with solid-state hydrogen nuclear magnetic resonance (SS-¹H-NMR) of MAPbl₃ films, which showed a downfield shifting of the N-H hydrogen peak (Figure 7b), corroborating greater shielding from H-bonding with F⁻. Using time-of-flight secondary ion mass spectrometry (ToF-SIMS), as seen in Figure 7c, the authors showed that the fluoride congregates near the surface of the film and near the interface between the film and substrate, though significant fluorine signal is exhibited throughout the thickness of the film. We note that these data agree with the assumption that fluoride ions occupy surface and grain boundary sites, of which there is a greater planar density at the top and bottom surfaces (which are effectively entirely grain surface area), while grain boundary sites comprise only a small areal fraction of the planar cross-sections of the interior of the film. The authors further characterized fluoride-perovskite interaction through DFT calculations using supercells of FAPbl₃ with Fsubstitution in various halide bulk and termination sites. In agreement with the assumptions voiced above, the authors report that a fluoride ion has a 3.5 eV energetic preference for occupying the halide site in a FAX terminal surface layer – i.e., the apical site of a terminal PbI₅F octahedron where the F⁻ is in the outermost FAX plane of the (FAI-PbI₂)_n-FAF_{terminal} perovskite structure (the position shown in Figure 4a) – over a bulk site or the site within the plane of Pb²⁺ and I⁻ ions in a flat PbI₂ terminal surface layer. In this favored terminal site, they report a charge localization for the F-coordinated Pb²⁺ ion attributed to the formation of a stronger ionic bond relative to I-Pb as well as an increase in the formation energy of a

FA vacancy of 0.43 eV relative to an FAI terminal layer, owing to the strong hydrogen bonding between N-H_{FA} and F⁻. According to the hypothesis we presented earlier, this strong termination bonding should ameliorate the surface vacancy-related deep trap states discussed in section II-A, as well as physically occupy vacancies that would otherwise present binding sites for H_2O and O_2 discussed in section II-B. Regarding surface deep trap prevention, the authors reported significant PV performance-related improvements, the first of which being longer photocarrier lifetimes measured by TRPL (Figure 7d). While CsFAMA-I, CsFAMA-Br, and CsFAMA-Cl films exhibited relatively similar carrier lifetimes to untreated CsFAMA measured by TRPL, CsFAMA-F films exhibited approximately double the carrier lifetime compared to that of the control. As further evidence of decreased trap density, CsFAMA-F samples showed a mitigation of hysteretic behavior between forward and reverse scans in J-V curves, which is typically ascribed to defect-related charge trapping [96]. Using admittance spectroscopy, the authors measured the trap landscape directly and reported a reduction in trap densities of 33% for CsFAMA-F films relative to the control, and analyses of transient photovoltage and photocurrent measurements yielded an increase of recombination lifetimes of 93% (in agreement with TRPL results) and a decrease of transport lifetime (or mobility enhancement) of 30%. The resultant relative PCE increase was 11%. Passivating surface trap sites also proved effective in preventing degradation. In humid ambient air, the PCE of the control device fell to about 50% of its initial PCE after 6,000 h, while the CsFAMA-F device retained 90% of its initial PCE after that time. The authors also monitored the relative XRD peak areas of the perovskite and Pbl2 over time while annealing at 85 °C in nitrogen followed by 100 °C in air, and all films exhibited similar rates of degradation except for CsFAMA-F which maintained a significantly higher fraction of the perovskite phase throughout (Figure 7e). As a mechanistic rationalization of these observations, we offer the speculation that if metal fluorides are capable of accepting strong M—F---H—N hydrogen bonds, as noted above, such an interaction would be expected to render the donor's proton less acidic, thus impeding the deprotonation step of the catalytic degradation cycle hypothesis of Walsh and co-workers, cited in section II-B.

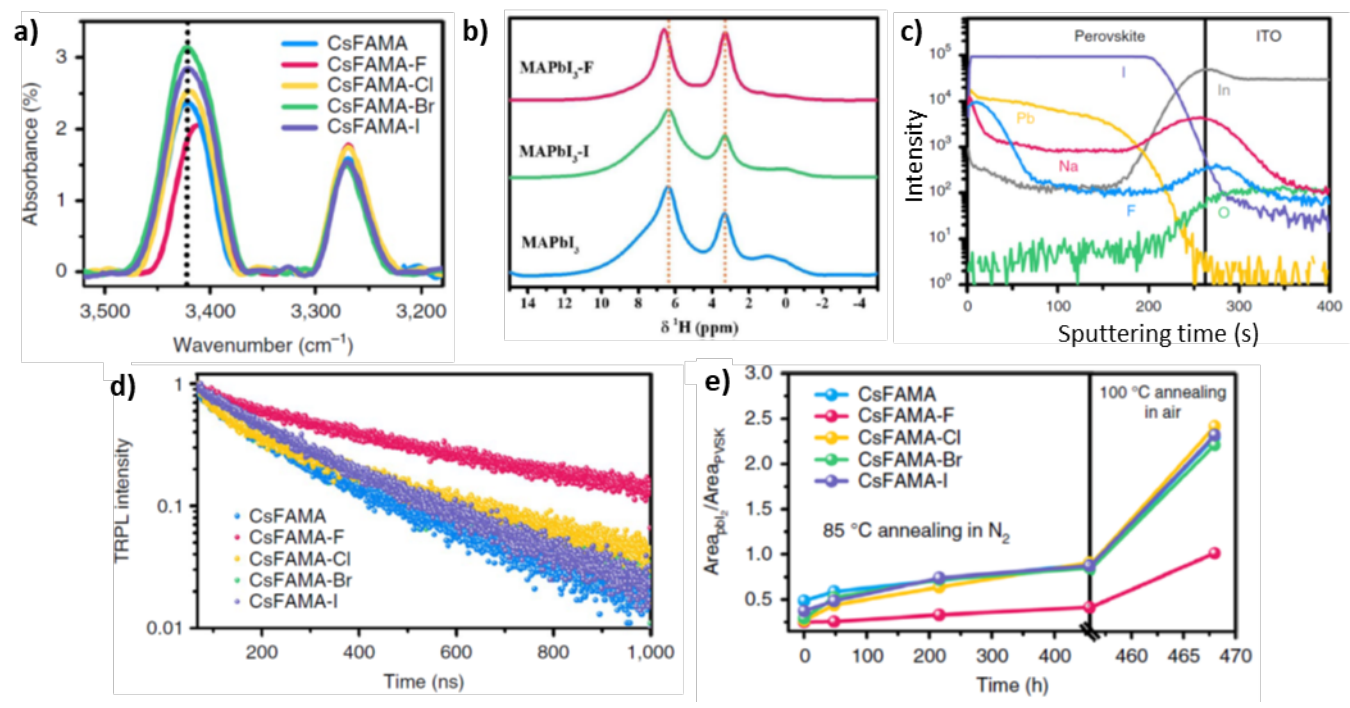


FIG. 7. Characterization of CsFAMA perovskite films with different NaX treatments (X = F, Cl, Br, I). a) FTIR spectrum regime of the N-H stretch of the organic cations. b) Solid-state ¹H-NMR for NaF- (red), NaI- (green), and un-treated (blue) MAPbI₃ films. c) ToF-SIMS elemental depth profile of CsFAMA-F film. d) TRPL decay measurements. e) XRD peak area ratios of PbI₂ and perovskite for untreated and NaX-treated CsFAMA films over time held at 85 °C in nitrogen for ~450 h followed by 100 °C in air for 12 h. Figures reproduced from reference [95], with permission. Copyright 2019, Springer Nature.

There are two other studies that offer possible routes to impart fluoride to the perovskite phase, though their main objectives focused on other aspects. Yi *et al.* [97] incorporated 5 mol % CsF in a two-step deposition of mixed FA/MA lead halide films. They treated the Pbl₂ precursor film with CsF, and then deposited the organic cation halide salts in the second step. They reported improvements in PV properties *via* trap reduction and dramatic stability enhancement including resistance to grain boundary degradation under UV light; however, we note it is ultimately difficult to disentangle the effects of Cs⁺ doping (their main objective) – which has been shown previously to improve PV performance and stability [98,99] – with F⁻ doping. Although the fluoride was initially incorporated into

the underlying Pbl₂ seeding layer, ToF-SIMS of the as-synthesized films show a similar profile as in the Li et al. [95] study discussed above, with fluorine content found mainly at the surface and film/substrate interface. We note that part of the difficulty in disentangling the effects of each dopant ion in Yi et al.'s study [97] lies in the uncertainties in the composition achieved with this fabrication method due to the solubility differences among the precursors. Consider that the Cs halide salt was incorporated in the precursor layer in an isopropanol (IPA) solution. The authors used CsCl, CsBr, and CsI to try to elucidate the importance of the anion, but they note that CsF is the only salt that is fully soluble in IPA. So while they reported much more advantageous results with CsF, one cannot be certain from this study alone that it is not simply an issue of solubility and film coverage. Still, SEM images showed that the morphologies of CsF-doped and CsCl-doped films were quite similarly uniform (unlike the much rougher CsBr- and CsI-doped films), and when comparing TRPL, it was found that the carrier lifetime of the CsCIdoped film fell -52% compared to the undoped control film, and the CsF-doped film carrier lifetime rose an astounding +106%. While any conclusion of the benefits of fluoride doping based on this study alone is confounded by the effects of Cs and differences in solubility, given the corroborating results in the NaF-doping study by Li et al. [95] discussed above, we believe a beneficial effect of fluoride anion substitution is strongly indicated. Clearly, further investigation is warranted, especially with a fabrication method that allows for more specific control of the fluoride incorporation without confounding variables. The authors of this study noted that they intentionally chose a two-step fabrication process for controllability and scalability and therefore selected CsF because of its superior solubility versus other Cs halide salts, but to our knowledge CsF has not previously been incorporated into MA/FA lead halide perovskites in a one-step method either. A one-step method would allow for better controls to disentangle the effects of Cs⁺- and F⁻-doping, as all of the CsX salts should be fully soluble in N,Ndimethylformamide (DMF).

The other relevant study, by Wu *et al.* [100], will be discussed in more detail in section V-A as its main focus was on fluorinating the external layers of a completed cell. However, it touches on a potentially powerful method to incorporate fluoride into the perovskite phase as well. In this study, the authors fluorinated cells using CF₄ plasma. The overlaying hole transport material (HTM) was the main target of the fluorination, and indeed the cells exhibited enhanced hydrophobicity and in turn enhanced stability. However, F-XPS mapping of the side of samples showed that fluorine was incorporated into every layer of the cell, including the perovskite phase. We are not aware of any other studies that use fluorinated plasma to modify the surface bonding of perovskites, though we highlight that plasma and vapor chemistries are promising routes to ensure complete mass transport to grain boundaries and surfaces.

Despite the small number of studies published on intentional fluoride incorporation into lead halide perovskites, there is a strong indication of the potential and a nascent understanding of the fundamental aspects of fluoride's role as a surface-terminating ligand and halide substitute.

C. Fluoride stabilization of black-phase CsPbX₃

The third family of perovskites discussed herein is the metastable $APbX_3$ ($A = FA^+$, Cs^+), with instability stemming from competing active and inactive phases due to ion size mismatch of the A-site, as introduced above. Fu *et al.* [101] recently reported stabilizing the photoactive black phase of $CsPbBrl_2$ using PbF_2 as a precursor substitute to Pbl_2 . They optimized the PV properties with an I:Br:F ratio of 1.78:1:0.22, where interestingly they stabilize a mixed-phase material of α - (black) and δ - (yellow) phases. At this F-loading, they observed a maximum J_{SC} . From TRPL and EIS, they cited both trap mitigation and improved carrier separation due to the band alignments in the mixed phase material. The result is a 20% relative increase in PCE *versus* the control. In terms of stability, under ambient conditions the control was reduced to 20% of initial PCE after 72 hours and 4% after 10 days, while after 10 days

the optimized F-containing film retained 70% of initial PCE with degradation only seen in the J_{SC} which the authors attributed to parasitic reaction with the silver electrode. The authors interpreted a reduction in the lattice parameter with increasing F content x to indicate bulk F-incorporation. However, given the evidence cited above for the difficulty of bulk F-incorporation, it would be interesting to follow up on this study with a quantitative determination of the perovskite phase composition, as the shrinking lattice parameter may alternatively be a function of the increasing Br⁻:I⁻ ratio of the precursor salts while F⁻ accumulates at grain boundaries.

D. Summary - Fluoride substitution

This section reviewed studies incorporating the fluoride anion into perovskite halides to prevent deep trap states and improve stability through tight bonding of the materials. This concept originated in the tin halides using SnF₂ as a source for excess Sn(II) to mitigate Sn vacancies, and it was soon reported that fluoride, too, benefits the stability of the tin halide perovskites by forming strong bonds with Sn and reducing the material's susceptibility to oxidation by atmospheric oxygen. Though the lead halides can benefit from the same bonding modulation by fluoride doping, there have been very few studies on fluorinated lead halide perovskites published in the literature, though those that have been published demonstrate significant improvements in PV performance and stability against PbI₂ degradation and phase instabilities. These studies warrant further investigation into fluorination effects and synthetic routes.

IV. FLUORINATED A-SITE CATIONS IN THE PEROVSKITE PHASE

In contrast to substitution at the *X*-site with F, this section provides an overview of perovskites incorporating fluorine-functionalized *A*-site organic cations. Evidence is reviewed below that fluorinated *A*-site cations can promote enhanced PV performance and stability by strengthening the intermolecular

bond between the cation and PbI₆ octahedral framework, increasing material hydrophobicity, and, in some cases, encouraging formation of efficient and stable so-called "mixed 2D-3D layered phases" (defined in detail in Section IV-B) due to the large size of most fluorinated cations. Outside of the context of fluorine incorporation, partial incorporation of bulky cations to form mixed 2D-3D layered perovskite phases is a widely-practiced technique for improving material stability; this forces a trade-off though, since layered perovskites have somewhat diminished PV performance. However, for the scope of this Research Update we will limit our discussion to studies focused on the unique outcomes when the bulky spacer cations are fluorinated. A review of general perovskites with mixed 2D-3D phases can be found in reference [102].

A. Intermolecular bonding modulation by fluorinated organic cations

As discussed in section III-B, increasing the intermolecular bonding between the A-site cation and the Pbl₆ octahedral framework can stabilize the perovskite against solvation, dissociation, and phase separation and transformation. While the previous section reviewed the evidence for direct hydrogen bonding to fluorine at the X-site, here we review the intermolecular bonding possible when highly polar fluorinated A-site cations interact with the Pbl₆ sublattice. Regarding the strength of intermolecular interactions of fluorinated cations, we note that fluorinated organic moieties can exhibit dipoles of several Debye in magnitude (compared to just over 1 Debye for simple methylamine) while dipolar and inductive effects of fluorination can lead to enhancement of hydrogen bonding strength by several orders of magnitude [103]. El-Mellouhi *et al.* [104] reported on the theoretical stability enhancement of MAPbl₃ with fluorinated MA⁺ (FMA⁺) as calculated by formation energy. Using DFT, they investigated the optimal location and extent of fluorine moieties in FMA⁺, and concluded that fluorine should replace a hydrogen of the methyl group (i.e., CH_{3-x}F_x-NH₃⁺, not CH_{3-N}H_{3-x}F_x) for the lowest system energy, and that the optimal F-content is with approximately 8% of hydrogen atoms replaced by F in the material, which

translates to one CHF₂NH₃* for every three MA*. The resultant structure increased the perovskite stability significantly. A summary of their analysis is as follows. The stabilization of FMAPbl₃ occurs due to an improved intermolecular bonding between FMA* and the Pbl₆ framework with associated structure distortion. The intermolecular bond is strengthened through the forced reorientation of the FMA* dipole under the influence of the electric field from one I*, pushing the ammonium group closer to an opposing I*, strengthening the ammonium-iodide intermolecular bond. They also noted that due to the electron-withdrawing nature of fluorine, the N-H bond is weakened, encouraging N*····H····I* bonding (Figure 8). They also reported that on the basis of DFT-minimized free energy pathways, 8% FMAPbl₃ increases the energy pathway for iodide vacancy migration from ~0.3 eV to ~0.5 eV, which translates to a decreased migration rate of three orders of magnitude at room temperature.

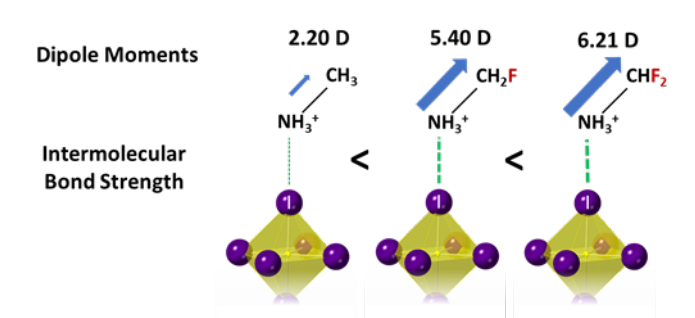


FIG. 8. The effect of a fluorine-induced dipole enhancement of fluoromethylammonium on the intermolecular bond strength between the cation and a PbI₆ octahedron. Dipole moments were obtained from reference [104].

Though the theoretical results are promising for stabilizing perovskite bonding through fluorinated cation modulation, there is not yet experimental evidence to demonstrate fluorinated cations in purely 3D perovskites. In their paper, El-Mellouhi *et al.* noted that there is considerable difficulty in synthesizing fluorinated methylammonium. However, larger fluorocarbon-ammonium cations are readily obtained and have been used to improve perovskites, though they modulate the perovskite structure to produce mixed layers of 3D and 2D perovskite phases. The next subsections cover these examples.

B. Fluorinated cations in 2D-3D mixed-dimensional perovskite phases

As discussed in the previous section, fluorinated organo-ammonium A-site cations can, in principle, improve lead halide perovskite PV performance and stability through strengthening intermolecular interactions within the lattice between the A-site and the PbI₆ octahedron, though this strategy has yet to be experimentally demonstrated due to the difficulty in synthesizing a fluorinated alkylammonium species small enough for the 3D perovskite lattice. However, the perovskite phase is simply the $n = \infty$ form of the more general Ruddlesden-Popper phases, denoted $A'_2A_{n-1}B_nX_{3n+1}$; in contrast, small n yields phases consisting of repeating layers of n unit cells of 3D ABX_3 perovskite terminated on both sides by A'X. The boundaries between these layers then consist of the interfacing of each layer's A'X termination, resulting in 2D spacer layers with a rocksalt-like crystal structure. The A' cation sites in these spacer layers constitute optimal sites for large, fluorinated cations.

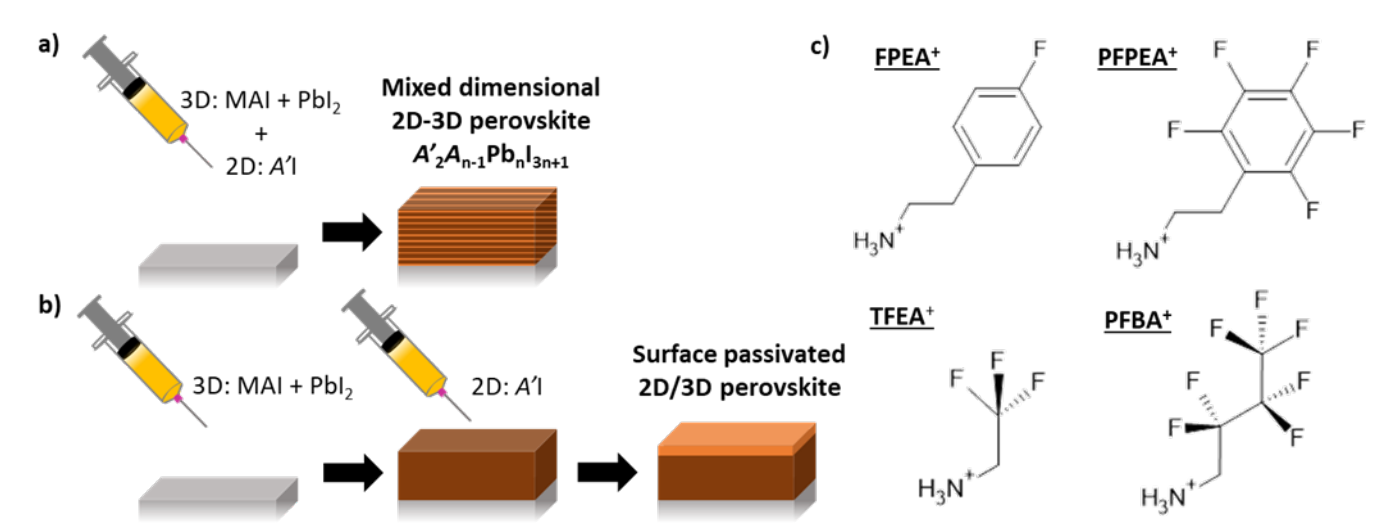


FIG. 9. Two approaches to 2D Ruddlesden-Popper stabilization of 3D perovskite phases. a) Perovskite precursor solution with mixed A-site cations (A is a 3D phase cation, i.e. MA^+ and A' is a 2D phase cation) for mixed dimensional 2D-3D perovskites. b) Two-step deposition of a 3D perovskite film followed by a surface treatment with 2D phase A-site precursor salt A'I. c) Examples of bulky, fluorinated 2D phase cations, including 4-fluorophenylethylammonium (FPEA $^+$), pentafluorophenylethylammonium (PFPEA $^+$), trifluoroethylammonium (TFEA $^+$), and 1H, 1H-perfluorobutylammonium (PFBA $^+$).

In these sites, the enhanced intermolecular bonding can still occur between the coordinated A' cation ammonium moiety and the 3D phase PbI₆ octahedron. Meanwhile, the A' cation fluorocarbon tails

within the spacer layer exhibit attractive van der Waals forces. Furthermore, it is well-established that fluorocarbons tend to have superior hydrophobicity to their hydrocarbon analogs. This further improves the ability for 2D spacer layers to inhibit transport of infiltrating species like water and oxygen. Mixed dimensional perovskite films of targeted n can be obtained by mixing controlled ratios of MA⁺ and a larger fluorinated cation in the precursor solution, as in Figure 9a.

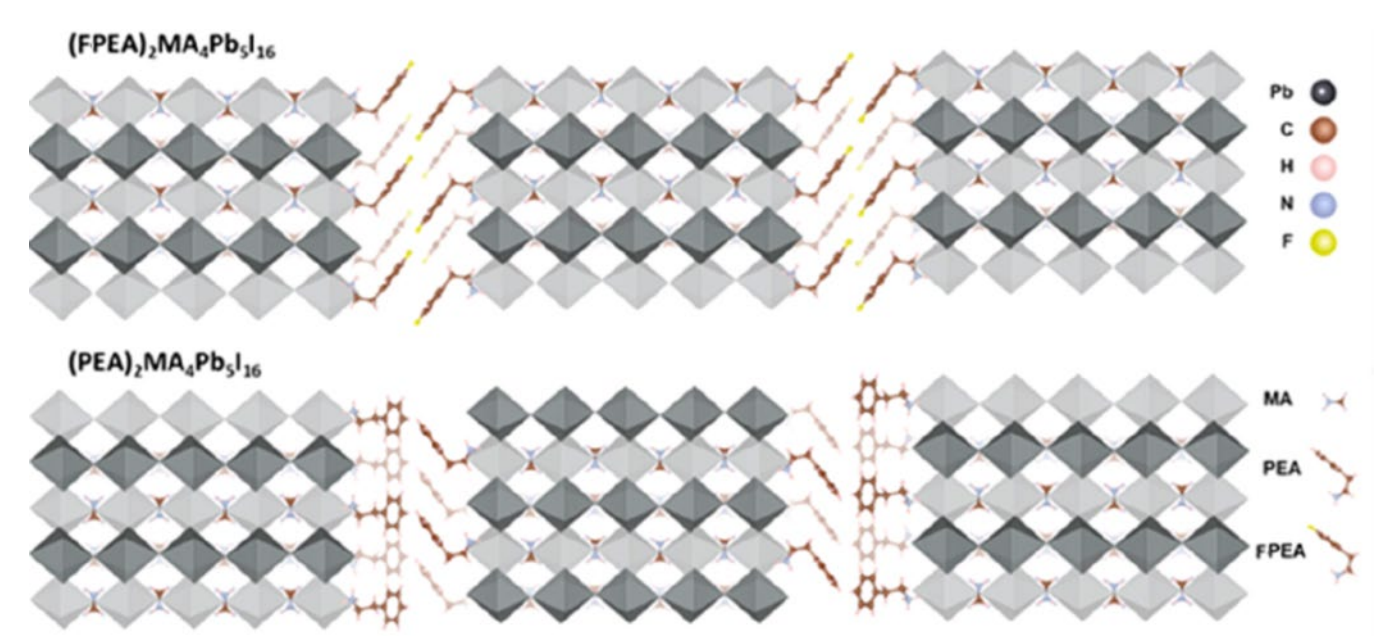


FIG. 10. Visual representations of the n=5 Ruddlesden-Popper phases of $A'_2MA_4Pb_5I_{16}$ ($A'=PEA^+$). Spacer layers are shown as a face-to-face ring alignment in the case of FPEA $^+$ (top) and face-to-edge ring alignment in the case of PEA $^+$ (bottom). Reproduced from reference [105], with permission. Copyright 2019, American Chemical Society.

One common 2D-spacer A-site cation used in mixed dimensional perovskites is phenylethylammonium (PEA⁺, C₆H₅-C₂H₄-NH₃⁺). Zhang et~al. [105] investigated the effects of functionalizing the benzene ring of this species with a fluorine in the para position to the ethyl ammonium moiety, employing 4-fluorophenylethylammonium (FPEA⁺, FC₆H₄-C₂H₄-NH₃⁺, Figure 9c). First, the authors compared films of n=1 Ruddlesden-Popper phase A'_2 Pbl₄ (A' = PEA⁺ or FPEA⁺). XRD showed that the interlayer spacing of FPEA-based films was slightly larger than that of PEA-based films. Interestingly, using time-resolved microwave conductivity measurements, they found a ~7-fold increase

in out-of-plane conductivity for the fluorine-functionalized film. Using single-crystal XRD measurements along with corroborative DFT calculations, the authors reported that in the spacer layers, the adjacent phenyl rings interface in a face-to-edge manner in PEA-based films, while in FPEA-based films the phenyl rings align in a face-to-face conformation as shown in Figure 10, reducing centroid distance and improving carrier transport through these layers in the out-of-plane direction. They attributed this conformational change to the polarization induced by the fluorine moiety which encourages pi interactions between the interfacing conjugated rings. With this information, the authors incorporated the cations into a mixed dimensional $n = 5 A'_2 MA_4 Pb_5 I_{16}$ ($A' = PEA^+$) Ruddlesden-Popper phase. Using conductive-tip atomic force microscopy (AFM), they showed a ~10-fold increase in surface conductivity for the fluorinated film. Shi et al. [106] studied the same fluorinated spacer cation and reported a relative crystallite size increase of 50% as well as a shift from plate and needle crystallite morphology in PEA⁺-based samples (Figure 11a,c) to only plate-like crystallites in FPEA⁺-based samples (Figure 11b,d). Though neither paper explicitly gives a reason, we believe it is logical to propose that the enhanced FPEA⁺ self-interaction promotes controlled and uniform crystallite growth. To probe PV performance, both papers showed a ~50% increase in carrier lifetime from TRPL, indicative of a reduction in trap density. Shi et al. measured a 70% decrease in trap states from PEA+- to FPEA+-based hole-only devices (Figure 12a), and Zhang et al. reported a decrease in J-V hysteresis (Figure 12b), which we note is consistent with a reduction of traps. We speculate that the difference could be explained by the more effective surface bonding of the FPEA⁺ cation compared to PEA⁺. These effects led to a relative 41% boost in PCE from PEA⁺- to FPEA⁺-based devices, with most improvement in the J_{SC} and fill factor (FF), according to Zhang et al. To address stability, Shi et al. demonstrated increased hydrophobicity for FPEA⁺-based devices than PEA⁺-based films with water contact angles (WCAs) of 62° and 41°, respectively (Figure 12c, inset). To demonstrate humidity stability, they also showed that under ambient conditions and 60% RH, FPEA⁺-based devices retained 93% of initial PCE over 500 h, while PEA⁺-based

devices retained 70% (Figure 12c). For thermal stability against cation sublimation, they showed that after annealing at 55 °C in a nitrogen environment for 500 h, the FPEA⁺-based device retained about 98% of initial PCE while the PEA⁺-based device dropped to 65% (Figure 12d). Liu *et al.* [107] also demonstrated similar success with a $A'_2A_8Pb_9l_{28}$ system (n = 9 Ruddlesden-Popper, A' = bulky spacer ions) while only substituting 10% of A' spacer cations with a similar fluoraryl ammonium species, demonstrating the effectiveness of this approach even in smaller dopant levels.

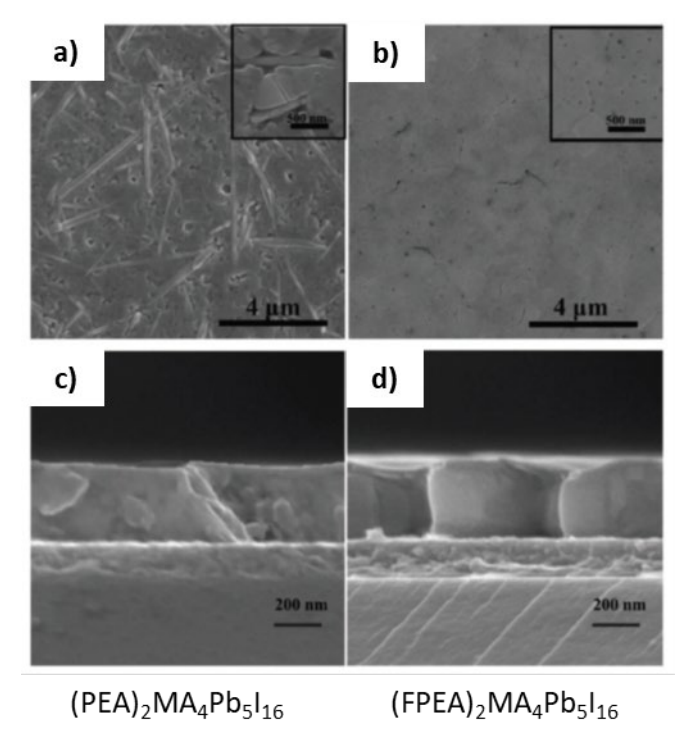


FIG. 11. SEM micrographs showing the topography and film cross-sections of $(PEA)_2MA_4Pb_5I_{16}$ [(a) and (c),respectively] and (FPEA) $_2MA_4Pb_5I_{16}$ ((b) and (d), respectively). Reprinted from reference [106], with permission. Copyright 2019, John Wiley and Sons.

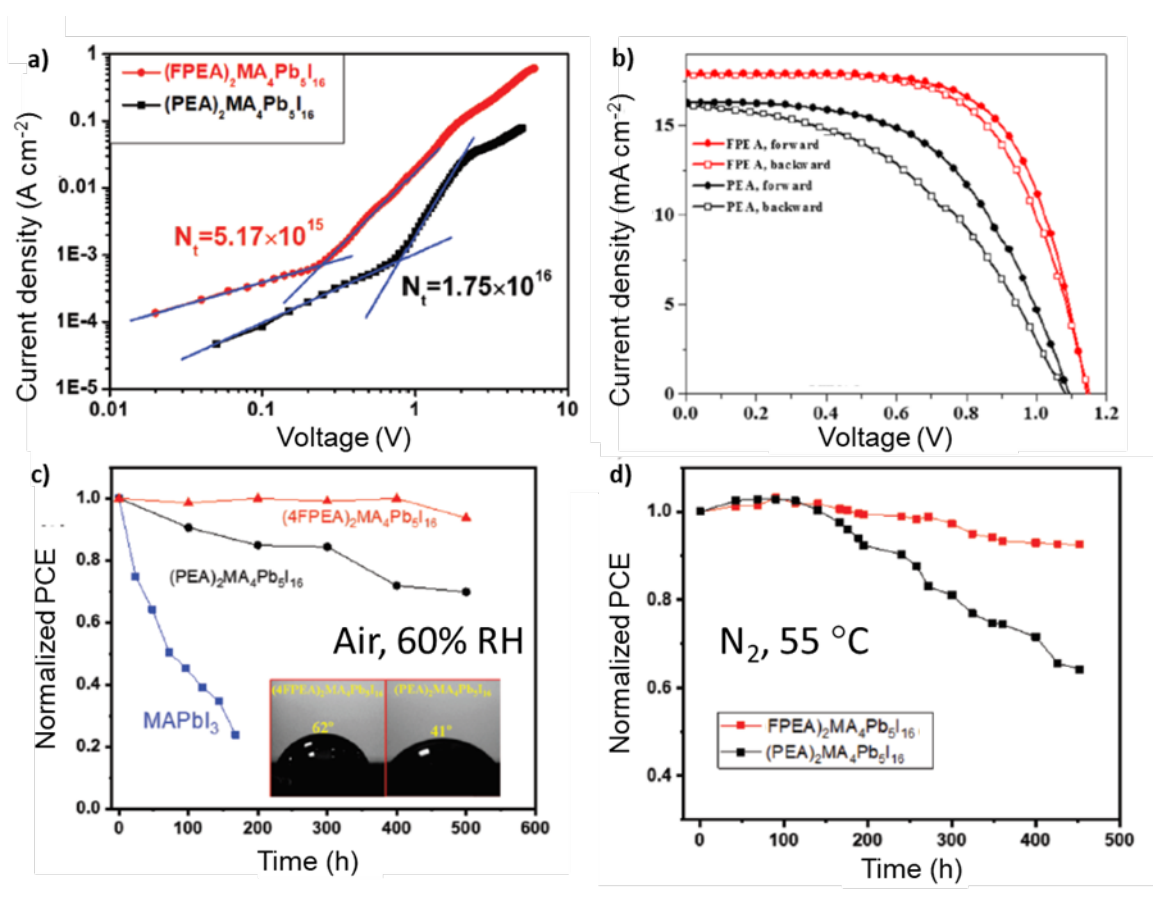


FIG. 12. PV and stability characterization of 2D-3D mixed phase $A'_2MA_4Pb_5I_{16}$ ($A' = PEA^+$: black data or FPEA+: red data). a) Dark I-V measurements of hole-only devices. b) *J*-V device characteristics. c) Normalized PCE over time while stored in ambient conditions at 60% RH, with initial WCA measurements inset and with MAPbI₃ device (blue data) for reference. d) Normalized PCE over time while stored in N_2 at 55 °C. (a), (c), and (d) are reproduced from reference [106], with permission. Copyright 2019, John Wiley and Sons. (b) is reproduced from reference [105], with permission. Copyright 2019, American Chemical Society.

C. Fluorinated cation surface treatments for 2D layer passivation

2D Ruddlesden-Popper phases have well-established stability advantages over 3D perovskites, however they also come at the aforementioned cost of efficiency due to increased band gaps as well as inhibited charge transfer stemming from their larger exciton binding energy and anisotropic conductivity. These effects can be balanced in mixed 2D-3D phases, but we know that stability issues tend to arise more prominently at surfaces. Consequently, some studies have focused on post-deposition, partial replacement of surface cations with larger F-containing cations, thereby forming thin layers of 2D Ruddlesden-Popper phase on top of an unperturbed 3D film, topochemically. Liu *et al.* [108]

treated a 3D perovskite film by immersion in a solution of pentafluorophenylethylammonium iodide, followed by an anneal. With the thin 2D passivation layer, they reported an almost 3-fold increase in carrier lifetime with TRPL. They described a faster hole-transport process from the perovskite to HTM, which they corroborated with EIS by measuring a lower charge transfer resistance than that of the untreated 3D perovskite device. They also reported an increased Voc and attributed it to this improved charge transfer as well as a reduction in nonradiative recombination at the perovskite/HTM interface. The authors measured a relative 9% increase in PCE for the treated perovskite. In terms of stability, under 1-sun illumination in ambient conditions, the 2D-passivated perovskite film retained an impressive 90% of initial PCE after 1000 hours, while the untreated 3D perovskite device fell to 43%. Interestingly, the authors also demonstrated that in EIS measurements with V > 850 mV, treated films exhibited less capacitance than untreated films, indicating a suppression of ion migration. We note that surfaces and grain boundaries are expected to be lower-barrier pathways for ion migration, and therefore it is sensible that passivation using the strongly-bonding cations of the 2D phase inhibits these pathways [109]. Using a similar approach with FPEA⁺, Ishikawa et al. [110] demonstrated 2D surface passivation of 3D perovskites by a brief soak in a solution of (FPEA)I. The authors reported successful trap passivation as evidenced by a 3-fold enhancement in PL intensity and almost doubling in average carrier lifetime measured by TRPL. They also reported a 10% enhancement in PCE, mostly due to an increase in V_{oc} which they attributed to the high conduction band minimum of the 2D Ruddlesden-Popper layer acting as an increased barrier to electron transport between the 3D perovskite and HTM.

So far in sections IV-B,C, we have only presented studies based on fluoro-aromatic FPEA⁺ and its close relatives. However, fluoroaliphatic cations have also proven beneficial for 2D surface passivation.

Xu et al. [111] formed a passivating 2D Ruddlesden-Popper layer on a 3D perovskite using trifluoroethylammonium for a spacer cation by dip coating. They measured over 33% trap density decreases in dark I-V measurements, with over a 50% increase in carrier lifetime as measured by TRPL.

As such, their EIS analysis corroborated a decrease in charge transfer resistance and an increase in recombination resistance for the treated films vs. the control films. They reported a 10% relative increase in PCE of treated films, and after 60 days under ambient conditions at 50% RH, treated films retained 88% of initial PCE while controls fell to 65%.

Similar results were reported by Zhao *et al.* [112] who treated perovskite films with perfluoroalkylammonium species of different carbon chain lengths with the optimal effects stemming from perfluorobutylammonium. We note that the authors did not structurally characterize an overlaying 2D phase in this study, but we include it here based on the similarity of their film treatment with the studies previously discussed in this section. They also measured longer carrier lifetimes in films and faster quenching in perovskite/ETM layered structures by TRPL, ascribing the effects to reduced trapassisted non-radiative recombination and improved charge transport. EIS showed an increase in recombination resistance. Stability was also greatly improved in this study. PCE of the control devices fell to 0% after 6 days in 50% RH while the treated devices retained 85% of initial PCE after 10 days.

D. Summary - Fluorinated A-site cations

Fluorinated spacer cations as additives in perovskite films have demonstrated effective improvements in PV function and film stability. Going further than capitalizing on the innate stabilization effects of 2D mixed phases in general, the fluorine moieties can modify cation dipoles to enhance intermolecular bonding between the cation and perovskite scaffold, improve intermolecular bonding between cation tails within the spacer layers to encourage interspace coupling, and support charge separation in the spacer layers which have historically shown large exciton binding energies. The results include improved morphology, enhanced PV performance from trap passivation and improved charge transfer, and greater humidity and thermal stability from improved hydrophobicity and bond strengthening. Additionally, studies of perovskite surface passivation via conversion to 2D phases with

fluorinated moieties have demonstrated similar improvements. While we feel that not enough data exist to compare the efficacy of mixed-dimensional films *vs.* surficial 2D layer formation, both have shown promising results in improving PV performance and stability.

V. LARGE- AND SMALL-MOLECULE FLUOROCARBON-BASED ADDITIVES FOR SURFACE PROTECTION AND PASSIVATION

Fluorocarbons have a long history in hydrophobic surface applications, which can be directly and indirectly applied to protecting perovskite surfaces from water attack and parasitic oxygen. This section will review some large-molecule (typically polymeric) and small-molecule fluorocarbon-based additives which have been applied to perovskite solar cells either as surface layers or as composite materials. The main stabilization effects highlighted herein target hydrophobicity as a means of physiochemical exclusion of water and oxygen, though stability and PCE improvements also stem from intermolecular interactions between the fluorocarbons and the perovskite to passivate surface defects, improve band alignment using the electron-withdrawing nature of fluorine, and enhance charge separation through permanent interfacial dipole moments.

A. Hydrophobic fluorocarbon layers in perovskite solar cells

The most straightforward approach to stabilizing perovskite halides against water and oxygen attack is to create a physiochemical barrier to their infiltration. Encapsulation is ubiquitous in solar cell manufacturing, and relies on purely physical means to protect cells, but perovskite solar cells can benefit from more intimate barriers that exploit hydrophobicity to not just seal the material from foreign species but also actively repel them. Hwang *et al.* [113] reported on an individual cell encapsulation technique that involved coating a completed cell with polytetrafluoroethylene (PTFE, $(C_2F_4)_n$, Teflon) *via* a solution precursor, with the architecture shown in Figure 13a. For comparison, they examined the

performance and stability versus an uncoated cell in which the perovskite layer was protected from the atmosphere only by the commonly-used overlaying hole-transport material (HTM) of Spiro-OMeTAD. This simple architecture yielded a device that retained 95% of its PCE over 30 days sitting in ambient indoor conditions while the control device efficiency depleted to 55% over the same timeframe. Furthermore, they were able to submerge the encapsulated sample in water for more than 15 minutes without visible degradation to PbI2 except for a thin border along the perimeter of the film where the PTFE layer did not protect the sides of the perovskite layer; the control sample changed from black to yellow (indicative of complete conversion to Pbl₂) in one second. The group reported an insignificant change in initial PCE of the two cells, indicating that the PTFE layer neither helped nor hindered the PV performance. Another promising example of overlayer encapsulation (Figure 13a) was reported by Bella et al. [114], who protected a complete cell stack with a UV-curable fluoropolymer loaded with common commercial fluorescent organic dye, Lumogen F Violet 570. The fluoropolymer provided hydrophobic protection, while the dye imparted luminescent downshifting (LDS) properties, effectively converting UV photons to red light photons, thereby protecting the perovskite from the UV-related degradation. The stabilization effects of hydrophobicity and LDS were disentangled by comparing samples with the coating only on the front surface with samples with the coating on both front and back surfaces. The samples were exposed to UV irradiation in air and constant 50% relative humidity (RH). The front-coated samples readily deteriorated to ~20% of initial PCE after 3 months in these conditions, while the frontand back-coated samples showed no significant depreciation over this time, showing the necessity of hydrophobic protection. To further demonstrate the efficacy of this treatment, the authors set doublycoated samples out on an outdoor terrace overlooking Turin, presumably with a glass of Dolcetto and old tales of summers spent in Tuscany, for the months of October through December, subject to the natural temperature ranges and weather of Northern Italy. Remarkably, the cells retained 95% of PCE

over this time. Similarly, the doubly-coated cells did not show appreciable degradation after being submerged in water for a full day.

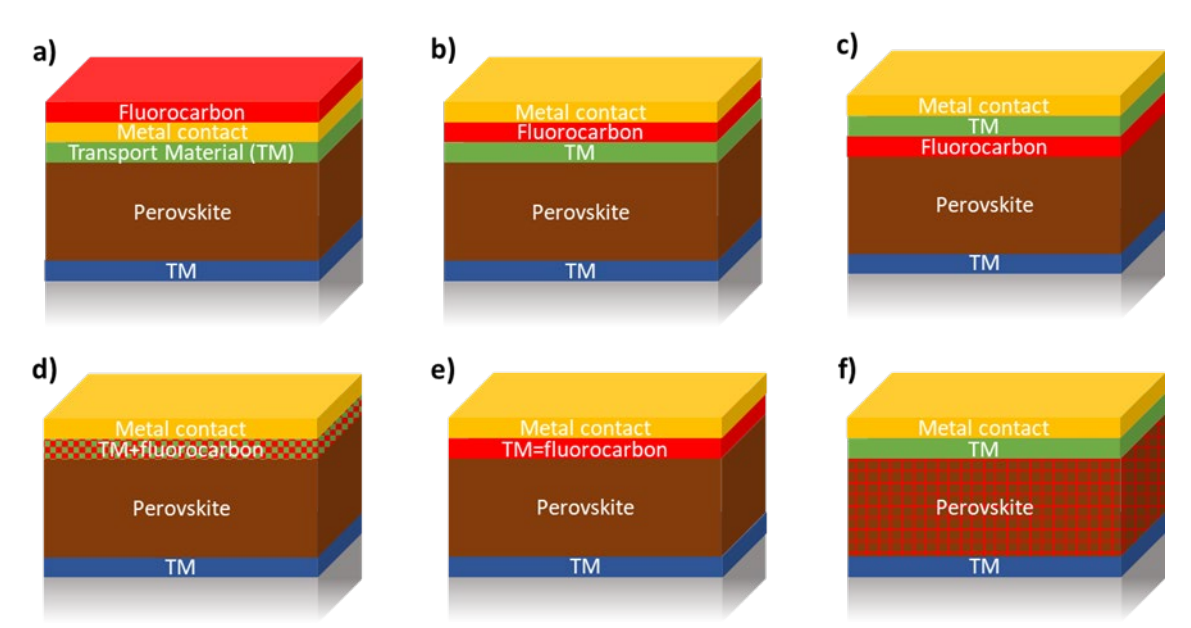


FIG. 13. Various configurations for inclusion of fluorocarbons in perovskite solar cell stacks. a) An external coating layer. (b) A fluorocarbon layer between the upper transport material (TM) and metal contact. (c) A fluorocarbon layer between the perovskite and upper TM. d) A TM embedded within a fluorocarbon. e) A fluorocarbon layer that serves as a transport material. f) A fluorocarbon composite within the perovskite layer.

Instead of coating a separate fluorocarbon onto a cell, the previously mentioned study by Wu *et al.* [100] simply fluorinated the surface of the HTM Spiro-OMeTAD in a completed cell stack through CF₄ plasma treatment, resulting in an architecture like that of Figure 13b in which the surface of the upper transition material serves as a fluorocarbon layer. After treatment, the hydrophobicity was greatly enhanced as measured through an increase of WCA from 72° to 116°, and XPS confirmed the presence of C-F bonding at the top and lateral surface of the Spiro-OMeTAD. While no significant difference in PV performance was noted, the stability was greatly improved. When held at the maximum power point under continuous 1-sun illumination in ambient conditions, the untreated film fell under 50% of its initial PCE in under one hour, while the treated film maintained 80% of its initial PCE after 100 hours. Even more impressively, after being submerged in water for 5 minutes, the treated film showed negligible degradation while the untreated film was completely converted to yellow Pbl₂. Kim *et al.* [115]

fabricated inverted perovskite solar cells with solution-deposited fluorine-functionalized graphene nanoplatelets as a similar protective layer atop the ETMs of their devices (architecture Figure 13b). They compared devices without the layer, with non-functionalized graphene nanoplatelets (with natural edge terminations of hydrophilic hydroxide groups), and with fluorine functionalized graphene (FFG) nanoplatelets in which edge terminations were designed to be hydrophobic C-F moieties. Graphene and FFG nanoplatelets are pictured in Figure 14. The FFG samples exhibited the most stable performance, with initial PCE about equal to that of the untreated devices, and retained 80% of their initial PCE after 30 days. Conversely, by the 15-day mark, the untreated devices had lost all PCE, and the non-functionalized graphene-based devices had been reduced to ~35% of their initial PCE. Graphene is appropriate for this application because it is conductive, so it will not appreciably hinder charge extraction between the perovskite and ETM layers. However, its degree of hydrophobicity is less than that of fluoropolymers.

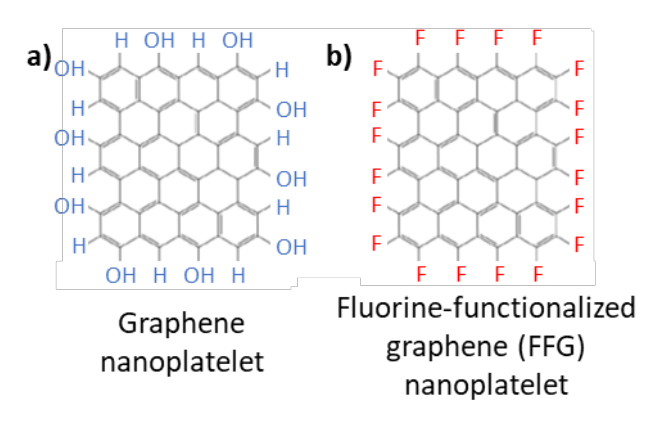


FIG. 14. Edge terminations of a graphene nanoplatelet (a) and fluorine-functionalized graphene nanoplatelet (b). Adapted from reference [115], with permission. Copyright 2017, American Chemical Society.

In the examples above, fluorocarbons served as surface layers atop the overlaying transport materials. They effectively protected devices from infiltrating species but had little effect on PV performance as they had no physical interaction with the perovskite layer. Alternatively, fluorocarbon layers can be incorporated inside the stacks. Liu *et al.* [116] developed a fluorinated copolymer

specifically suited for hydrophobicity and thermal and mechanical durability, which they deposited between the perovskite layer and the HTM (as in the architecture pictured in Figure 13c). In this configuration, the insulating fluoropolymer can be a barrier to charge extraction through the HTM, and so the layer thickness has direct consequences on PV performance. An optimized layer thickness was determined to be 25 nm based on PCE. The authors reported no change in morphology of the individual cell layers and concluded that the optimized fluoropolymer layer was responsible for this relative 20% boost in PCE, though they did not offer an explanation. From the discussion of surface state passivation in section II-A, we speculate that the fluoropolymer may be coordinated to perovskite surfaces, thereby passivating surface defect states. The improvement in stability is also stark, with the optimized fluoropolymer device retaining 80% of initial PCE over 100 days while the untreated sample dropped to 10% initial PCE in 21 days.

B. Hydrophobic fluorocarbons within charge transport layers

Rather than in distinct layers, fluorocarbons can form a composite with, or act directly as, ETMs and HTMs. Lei *et al.* [117] fabricated inverted perovskite solar cells using a composite porous PTFE scaffold loaded with room-temperature sputtered ZnO (in the architecture shown in Figure 13d) and compared these to controls with i) pure ZnO and ii) organic PCBM as ETMs (Figure 15a). The PTFE:ZnO ETM devices had a relative initial PCE 10% less than the PCBM-based devices. However, in 60% RH stability tests, the PTFE:ZnO devices showed no degradation in XRD patterns over 21 days, while the PCBM-based devices completely degraded by day 18. In long-term stability tests shown in Figure 15b, the pure ZnO ETM devices saw PCE fall to 75% of their original value in 2 months, while it took PTFE:ZnO devices 6 months to fall to that value. The authors noted that oxide materials are stable physical barriers to gaseous species, but oxides have hydrophilic surfaces, which will still facilitate slow Knudsen diffusion

of water. Comparatively, the physiochemical repulsion of water by the composite ETM hinders water penetration more effectively, as evidenced by much larger WCA (Figure 15a, insets).

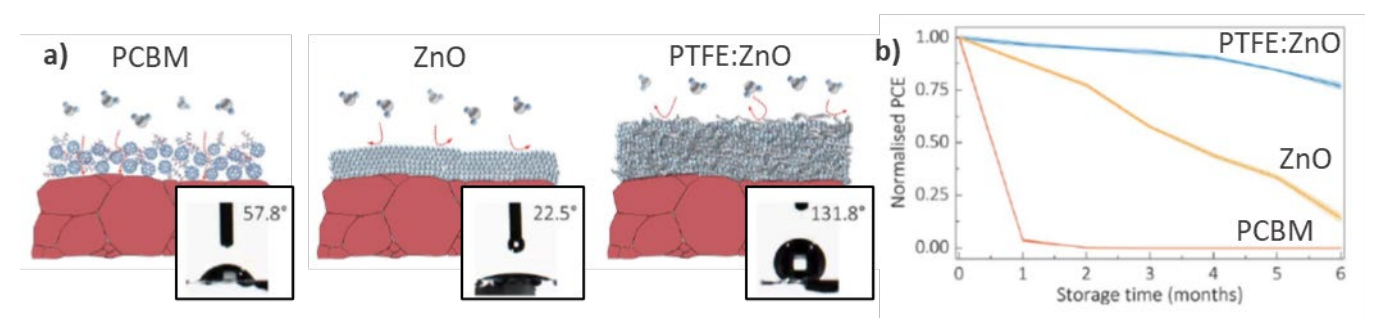


FIG. 15. a) Various HTMs: PCBM, ZnO, and ZnO embedded in a PTFE scaffold (PTFE:ZnO), and illustrations of their interactions with water. Insets are WCA pictures and measurements taken on films with each type of HTM overlaying the perovskite. b) Normalized PCE versus storage time under ambient conditions for films overlaid with the three different HTMs. Adapted from reference [117], with permission. Copyright 2019, The Royal Society of Chemistry.

On the flip side, literally, fluorocarbons have proven effective as HTMs. One of the most common HTMs is the organic large-molecule Spiro-OMeTAD. However, it has been known to be susceptible to pinhole formation and atmospheric sensitivity [118]. An attractive alternative is the polythiophene material known as P3HT, which offers high hole mobility and improved humidity resistance. Unfortunately, it also has a shallow valence band maximum (VBM), and which results in poor band alignment with perovskite absorbers, thereby limiting $V_{\rm OC}$ and overall PCE [119]. Jeong *et al.* [120] proposed a fluorinated polythiophene alternative, known as FEH, as an HTM (as in architecture Figure 13e) with very promising results. The structures and band alignments of Spiro-OMeTAD, P3HT, and FEH are displayed in Figure 16a,b. In terms of stability, cells with FEH as the HTM outperformed those with Spiro-OMeTAD and P3HT HTMs, shown in Figure 16c. After 100 h in ambient atmosphere, the FEH devices retained ~85% of initial PCE, which remained constant for the subsequent 400 h (the end of the experiment). Also being relatively hydrophobic, the P3HT device followed a similar trend, retaining ~80% of initial PCE, and remaining constant over the next 400 h. In contrast, the Spiro-OMeTAD device fell to ~55% of initial PCE after 500 h and still showed signs of slow degradation at that point. The trends track

with the hydrophobicity of the HTMs, measured by water contact angle (WCA), with WCA of FEH > P3HT > Spiro-OMeTAD (Figure 16c, inset). While both thiophene HTMs performed similarly well in the longterm stability test, FEH very clearly outperformed P3HT by a relative 70% advantage in PCE. This is described by a different effect owing to the presence of fluorine. Recall that P3HT underperforms other HTMs like Spiro-OMeTAD in PCE due to a shallow VBM. Functionalization with fluorine withdraws electron density from the polythiophene backbone, effectively lowering the VBM and achieving better band alignment with the perovskite, thereby preserving high Voc. This VBM-tuning effect upon fluorination has been demonstrated for perovskite solar cells in another polymer HTM system, poly(triarylamine), [121] as well as in a porphyrin-based HTM [122]. Furthermore, in comparing Jeong et al.'s FEH devices to Spiro-OMeTAD devices, FEH devices show a relative 7% advantage in PCE over the Spiro-OMeTAD devices, stemming from more efficient charge extraction (measured by TRPL) and a higher FF, indicating lower series resistance and/or higher shunt resistance in devices. To explain this, we can look at the film morphologies. The authors reported pinholes in Spiro-OMeTAD films, whereas no pinholes form for FEH films. FEH, especially compared to P3HT, forms very uniform and complete films, which can also be attributed to the fluorine moieties. It has been reported that the fluorinated backbones in polythiophenes contribute to improved conjugation in the backbone structure, allowing enhanced intermonomer π - π interactions, and thereby causing the equilibrium angle of rotation between neighboring thiophene rings in the backbone to change from 17° in HEH (the unfluorinated analog of FEH) to 0° in FEH, establishing a "flat" chain for efficient molecular packing [123]. This effect is similar to that discussed in section IV regarding improved intermolecular interfacing of fluorinated cationic spacer layers in mixed dimensional perovskites.

Another study by Jeong *et al.* [124] (different researchers from the previous study), focused on fluorinated derivatives of Spiro-OMeTAD. They added a fluorine to four of the methoxyphenyl groups, one derivative with fluorine atoms bonded *meta*- to the nitrogen, and one with fluorine bonded *ortho*-

to the nitrogen. Both yielded enhanced efficiency but the meta- derivative, "Spiro-mF," produced champion cells. Compared to traditional Spiro-OMeTAD, the Spiro-mF devices had a relative increase in PCE of 5.9%. The authors attributed the increase in V_{OC} to reduced band offset at the interface with the perovskite, as a consequence of fluorination rendering the VB more negative in energy. They attributed increases in J_{SC} and FF to improved packing and charge transfer due to molecular flattening with fluorination, similar to the effect described in the paragraph above, which they supported with molecular dynamic simulations.

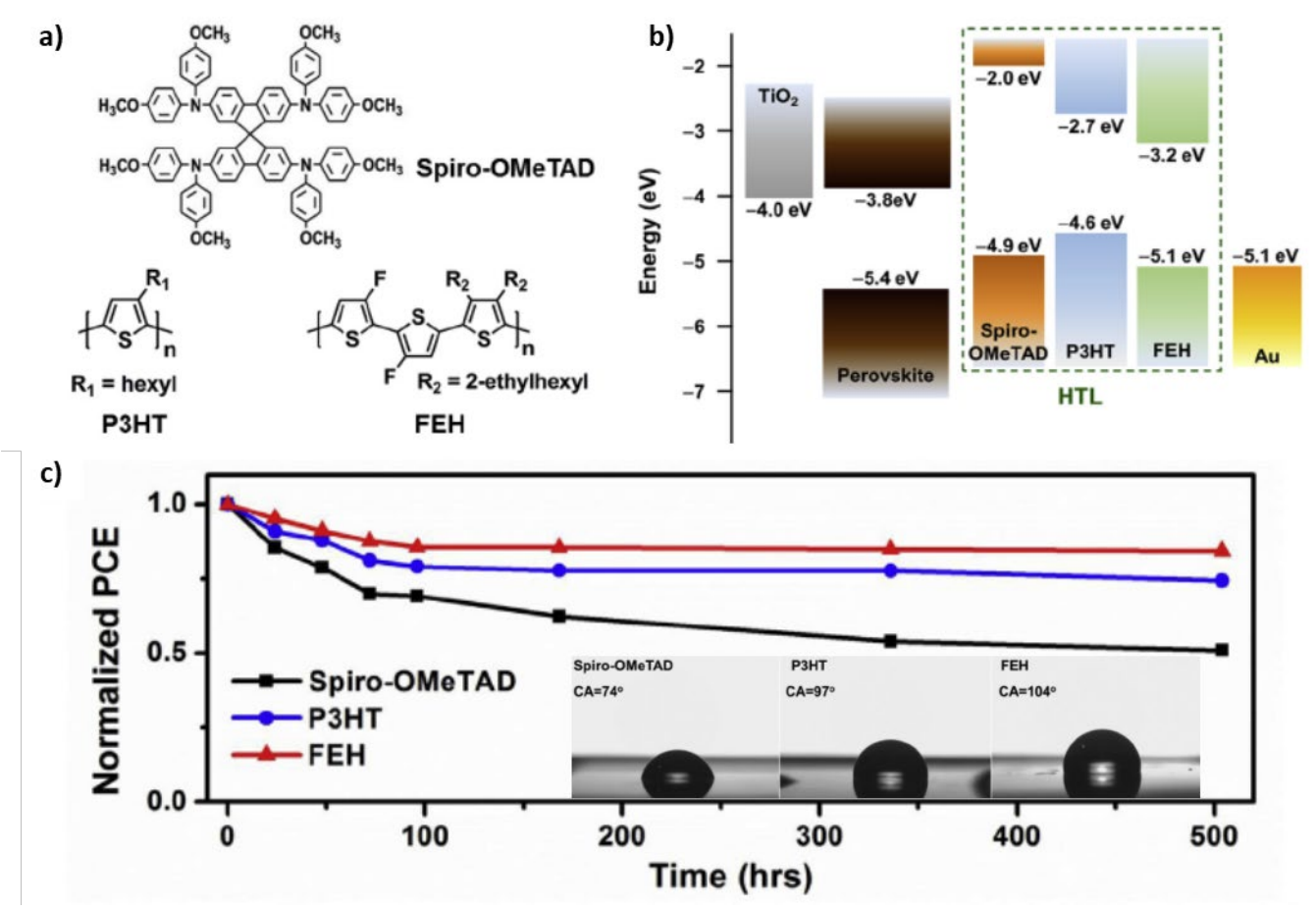


FIG. 16. a) Molecular structure of HTMs Spiro-OMeTAD, P3HT, and FEH. b) Band alignments of perovskite solar cell components, comparing that of the three HTMs. c) Normalized PCE measured over time in ambient conditions. Inset: WCA images and measurements of perovskite films with overlaid HTMs. Figures reprinted from reference [120], with permission. Copyright 2019, Elsevier.

WCA measurements showed that the Spiro-*m*F (81.5°) is slightly more hydrophobic than Spiro-OMeTAD (76.2°), and after 500 hours uncencapsulated in 50% RH, Spiro-OMeTAD devices fell to 60% of initial PCE and evolved a PbI₂ peak in XRD while Spiro-*m*F devices retained more than 87% of initial PCE with no XRD evidence of PbI₂.

C. Fluorocarbon-perovskite composite absorbing layers

In the examples discussed so far, fluorocarbons have been implemented as layers distinct from the perovskite. However, as the benefit of perovskite-fluorocarbon interfacing has been demonstrated, it follows that another potential route is to combine fluorocarbons in the perovskite precursor and deposit the composite as a single layer, as seen in Figure 13f. This motif differs conceptually from that discussed in Section IV as these molecular additives do not compete for A-site occupancy, but instead interact with the perovskite through intermolecular bonding. Valero et al. [125] developed one small molecule and two polymers with perfluorinated alkyl moieties, shown in Figure 17a and labeled D1-D3, to serve as additives to the perovskite precursor solution in a solar cell. The PV performance was not substantially changed compared to the control devices, though the group saw improvement in the stability of the devices, particularly with the small molecule species. In short-term bias testing at the maximum power point in air, seen in Figure 17b, the control device showed catastrophic failure after \sim 80 minutes. Conversely, the device with a small molecule additive maintained more than 90% of initial power output after that time. In long-term air stability tests under 50%-67% relative humidity (Figure 17c), the control device fell to ~50% of initial PCE after 16 days, while the device with small molecule additive retained ~80% of initial PCE after that time. They attributed this effect to the improved hydrophobicity, as well as improved morphology. They reported slight grain enlargement, grain boundary fusion, and smoothing of the film surface with the use of their additives.

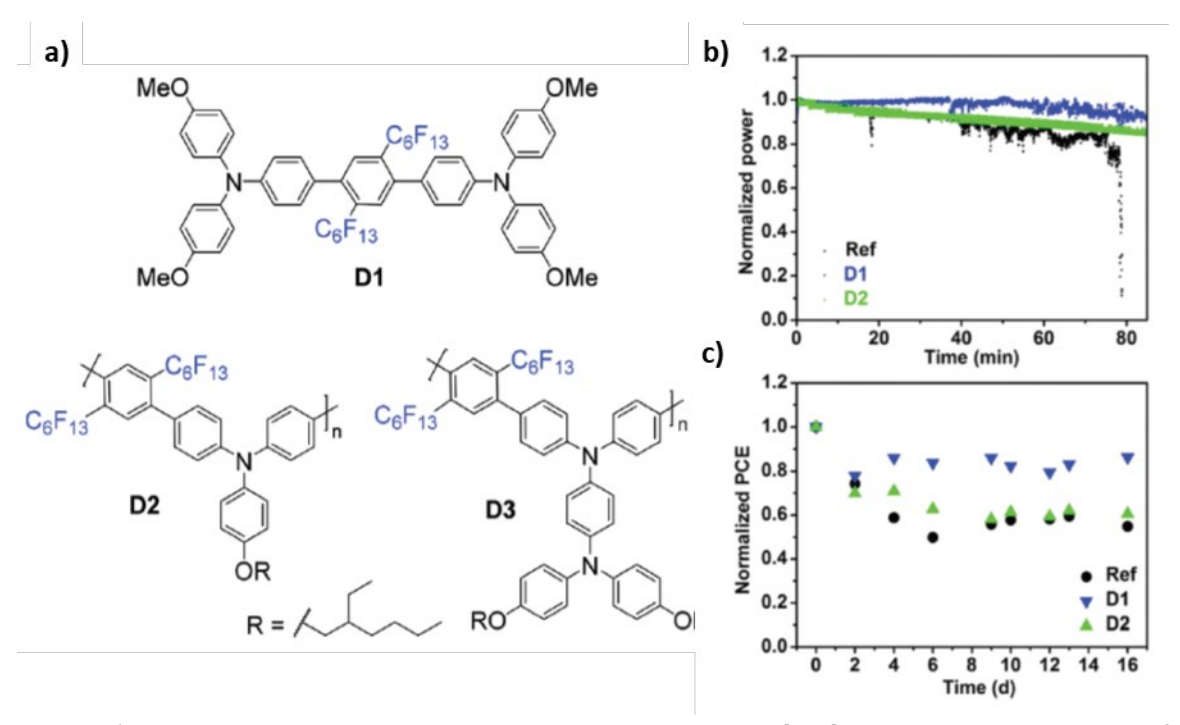


FIG. 17. a) Fluorocarbon molecule additives developed by Valero *et al.* [125] incorporated into perovskite films. b) Normalized power at the maximum power point measured in air over time for an untreated perovskite film, and films treated with D1 and D2. c) Long-term air stability tests showing normalized PCE over time of devices stored in 50-67% relative humidity. Figures reprinted from reference [125], with permission. Copyright 2019, The Royal Society of Chemistry.

For mechanistic insight, we can turn to a study by Zhang *et al.* [126]. The authors added a copolymer of vinylidene fluoride and hexafluoropropylene (PVDF-HFP) as a hydrophobic perovskite-phase additive. While they did not report on stability effects, after optimization of the copolymer concentration in the precursor solution, cells showed a 35% relative increase in PCE over the pure-perovskite control, mainly seen in J_{SC} (24% increase) and FF (10% increase). The authors attributed this to improved film morphology, which they showed for control films and for films with increasing concentrations of additives. Upon additive concentration optimization, they observed a smoothing and improved uniformity of the film, resulting in fewer grain boundaries and less perovskite surface area. The authors also investigated the mechanism of this morphological control. It has been reported that additives (one being the solvent dimethyl sulfoxide, DMSO) can improve film morphology by forming complexes with precursors, which slows growth kinetics and leads to smoother, more uniform

films [127]. While crystallization tends to be performed at elevated temperatures (above 100 °C) in a matter of minutes, Zhang *et al.* tracked the progression of intermediate MA₂Pb₃I₈(DMSO)₂ in films crystallized at room temperature over several days in an inert environment. Figure 18a shows the XRD pattern for freshly spun films with (green) and without (black) PVDF-HFP additive. Peaks marked "#" correspond to the DMSO-complex intermediate. The peak marked "*" corresponds to the perovskite peak. After 48 hours in a glove box, the XRD patterns of the films evolved to those shown in Figure 18b. While films spun without the fluoropolymer additive converted completely from the intermediate to perovskite after 48 hours, films spun with fluoropolymer additive showed drastically slowed conversion and still more prominently featured the intermediate peaks in XRD. Additionally, in comparing absorption measurements of precursor solutions with and without PVDF-HFP as well as that of pure PVDF-HFP, shown in Figure 18c, they found an absorptive tail in fluoropolymer additive solutions which could not be attributed to either the intermediate or the pure fluoropolymer, possibly indicating a complexation of the intermediate by the fluoropolymer.

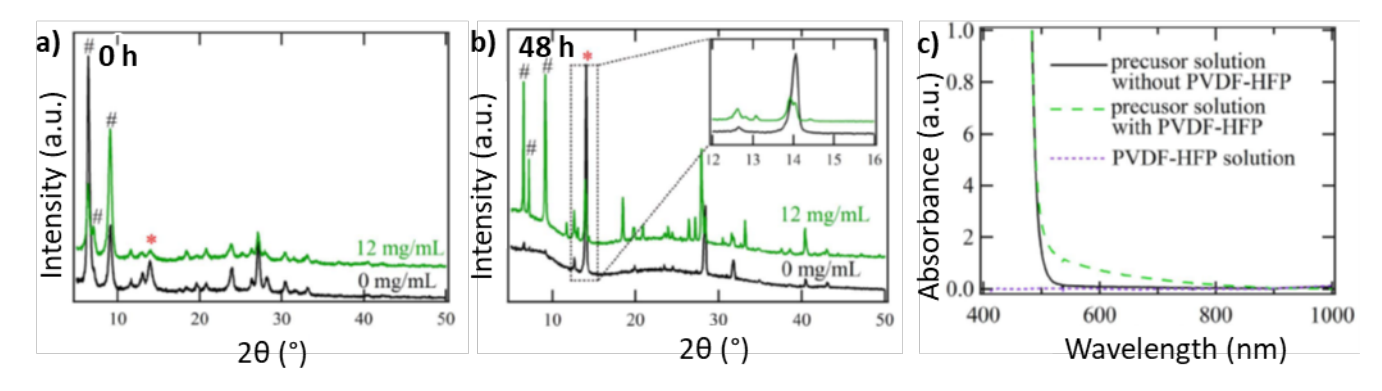


FIG. 18. a) XRD of precursor film immediately after depositing on the substrate of untreated perovskite precursor solution (black) and PVDF-HFP composite precursor solution (green). b) XRD of films 48 h after depositing on substrates, having been stored at room temperature in a glove box. In (a,b), peaks marked "#" indicate the MA₂Pb₃I₈(DMSO)₂ intermediate, and the peak marked "*" indicates the perovskite structure. c) Absorption spectrum of the perovskite precursor solution (black), the PVDF-HFP solution (purple), and the composite precursor solution (green). Figures reprinted from reference [126], with permission. Copyright 2017, Elsevier.

We saw in the last example that fluorocarbon additives can play an important role in controlling morphology *via* crystallization kinetics through interaction with perovskite precursors, but where do the

additives end up? Moriya et al. [128] included a perovskite precursor solution additive of a copolymer of vinylidene fluoride (-CH₂-CF₂-) and trifluoroethylene (-CHF-CF₂-) (P(VDF-TrFE)). Versus the control, the authors measured a 34% relative increase in average device PCE with the use of the additive, as well as a substantial reduction in PCE standard deviation, indicating that the use of additives yields more consistent devices. Once again, the PV performance enhancement was seen in increased J_{SC} and FF. (And again, it is worthy to note that additive concentration optimization is necessary to maximize the benefits of the additive films while minimizing the detrimental insulating nature of the fluoropolymer.) Though they did not report film morphology comparisons to the control, they did demonstrate decreasing film roughness with increasing additive concentrations. To answer the afore-asked question, the authors used XPS to detect fluorine's presence on the surface of the film. After etching a few nanometers from the film surface, they observed the total disappearance of the F 1s peak from the XPS spectrum, leading them to conclude that the fluoropolymer self-assembles as a surface layer during crystallization. However, while it is clear from the unchanged XRD pattern and absorption spectrum that the fluoropolymer is indeed totally excluded from the perovskite phase during crystallization, it is our belief that the fluoropolymer is likely to exist at all grain surfaces throughout the perovskite film and not as only a self-assembled top layer. Considering the aspect ratio and available surface sites for the fluoropolymer at film's exterior versus grain boundary sites in the film interior, it agrees with the XPS that the fluorine content inside the film would potentially fall to levels below the noise level for XPS detection.

As one further indication of the interaction between the fluoropolymer additive and perovskite phase, Jia *et al.* [129] incorporated P(VDF-TrFE) into a perovskite film and demonstrated an additional benefit to the fluoropolymer. PVDF and its copolymers are ferroelectric species, owing to the strong dipole imparted by C-F bonds and ordered crystallinity. In this study, the authors demonstrated ferroelectric coupling between the fluoropolymer and perovskite through piezoresponse force

microscopy and P-E curves. As an exciting proof of concept, the authors took fluoropolymer-loaded perovskite films, poled them for 10 minutes (positive/reverse bias and negative/forward bias), and then deposited remaining layers to complete cells. In characterizing the resultant cells, they reported on $V_{\rm OC}$ as well as extraction lifetimes. Positively-poled films outperformed unpoled films, which in turn outperformed negatively-poled films, having larger $V_{\rm OC}$ and FF, and faster charge extraction lifetimes, an effect ascribed to internal electric field tuning.

D. Fluorinated small molecule surface treatments

As briefly mentioned in section II-A, one can also specifically target surface states by adsorbing small-molecule ligands. As we show below, fluorinated moieties are a promising choice for such ligands, for many of the reasons described so far in this Research Update. Yang et al. [54] mixed a fluorinated perylenediimide (F-PDI) passivating molecule into the antisolvent used to crystallize perovskite films during the spin deposition process. The molecule, shown in Figure 19a, included perfluoroalkyl moieties to increase hydrophobicity and to hydrogen bond with the A-site ammonium cation of the perovskite as well as carbonyl groups to coordinate to lead dangling bonds. Through XPS and IR spectroscopy, the authors reported a downshift in Pb 4f electron binding energies (Figure 19b) and a shift in the N-H stretch to lower frequency (Figure 19c) with F-PDI treatment, respectively, supporting the existence of intermolecular bonding interactions. Though not highlighted by the authors, we also note nontrivial changes in the IR spectral range typical of C-F bond vibrations, indicated by the green rectangle in Figure 19c. Further controlled experiments focusing on this wavenumber regime could shed light on the nature of fluorocarbon interaction with perovskites. The treated films exhibited improved coverage and fewer pinholes than the control films, indicating a kinetic effect on crystallization by the ligand similar to that seen in the fluorocarbon additives discussed previously in this section. The F-PDI treatment improved PCE relative to controls by 19% with double the carrier lifetimes. Using dark I-V measurements, they also reported a 16% decrease in traps in hole-only devices, and a 50% decrease in traps in electron-only devices. Stability was also significantly enhanced, with unencapsulated devices in air at room temperature and 50% RH retaining 80% of initial PCE after 30 days for treated samples vs. only about 10% of initial PCE retained for control devices, shown in Figure 19d as dotted-line data (a similar comparative trend was obtained for devices in N₂ atmosphere at slightly elevated temperature, also shown in Figure 19d as solid-line data).

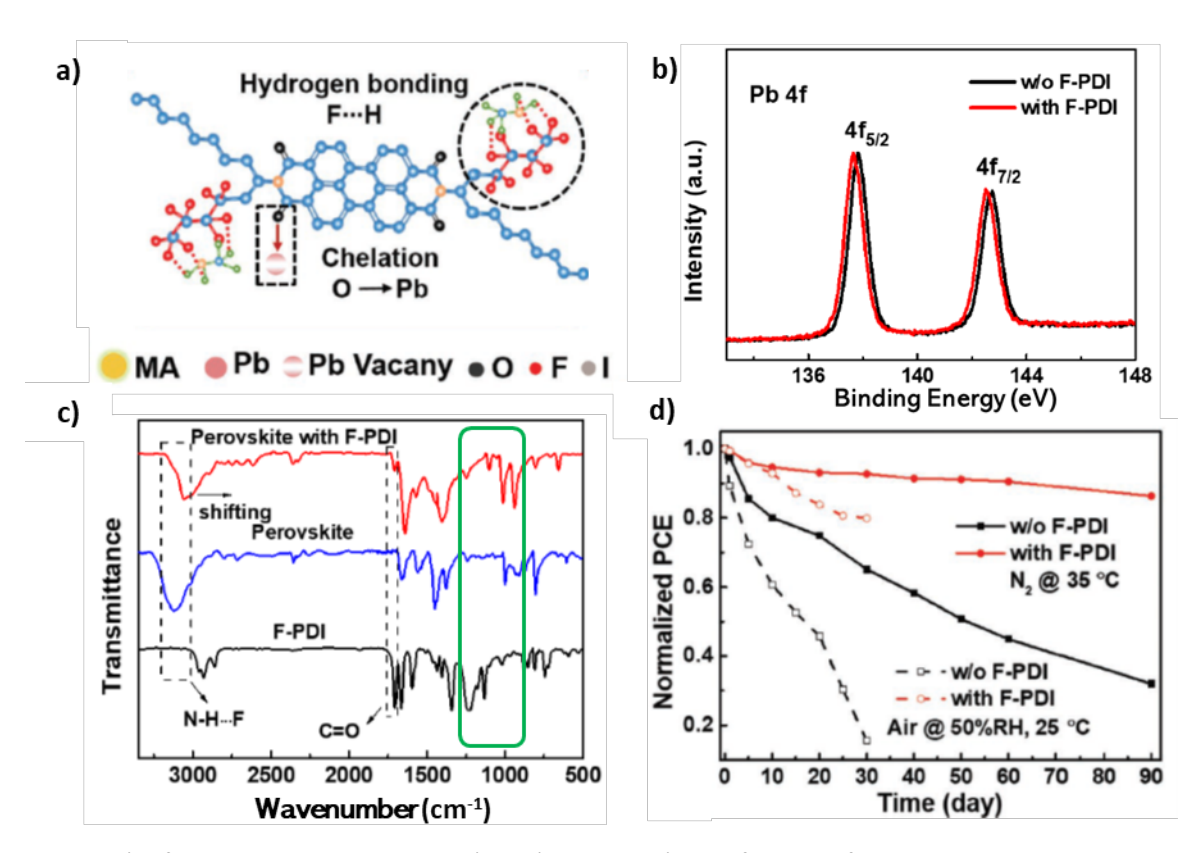


FIG. 19. a) A fluorinated perylenediimide (F-DPI) additive. b) XPS of the Pb 4f binding energy regime measured from films with (red) and without (black) F-DPI additive. c) IR transmittance spectra of F-DPI (black), pure perovskite (blue), and perovskite with F-DPI additive (red). We have added a green rectangle to low wavenumber region for discussion in the text. d) Normalized PCE versus time measured from devices with (red) and without (black) the F-DPI additive. Open circles and dotted lines represent devices held in conditions of open air and 50% RH at room temperature. Closed circles and solid lines represent devices held in conditions of N₂ atmosphere and 35 °C. Figures reproduced and adapted from reference [54], with permission. Copyright 2019 John Wiley and Sons.

In the example above, the surface treatment ligand was mixed into the antisolvent for the crystallization step, which begs the question: is there an ideal step during which to apply the passivating

ligand? Guo et al. [130] treated perovskite films with 1H,1H-perfluorooctylamine (PFA, shown in Figure 20a), with the amine head group acting as a Lewis base to coordinate to the perovskite and a perfluorooctane tail to exploit superior hydrophobicity for protection from water. They tried several methods of inclusion. The incorporation of additive into film precursor solutions severely compromised the final film morphology, while in contrast, two successful routes were i) incorporation of PFA in the antisolvent that was used to crystallize the perovskite during the deposition process, and ii) spin coating PFA onto preformed perovskite. Through XPS and SEM-EDS, fluorine was observed on the surfaces of both films, but throughout the depth of the film (likely localized to grain boundaries [GB]) only for films processed by method (i). Therefore, we will refer to these processes by their passivated regions: MAPI:surface+GB, and MAPI:surface. These scenarios are illustrated in Figure 20b. Both PFAincorporated films greatly outperformed the control films in terms of PCE and stability. However, the interesting comparison here is between MAPI:surface+GB and MAPI:surface. To illustrate the effects on PV performance, when champion devices were compared among the treated samples and controls, PCE relative to the control increased by 14% for MAPI:surface and by 27% for MAPI:surface+GB; device PCE statistics are shown in Figure 20c. Part of this difference was attributed to an improved film morphology. MAPI:surface films showed similar surface roughness to control films. However, MAPI:surface+GB films, where the passivating molecule was included in the crystallization antisolvent, boasted a 60% decrease in roughness from the control (11.0 nm versus 27.2 nm). The rest of the PCE increase can be accounted for by superior trap passivation when grain boundaries are also passivated. Relative to the control, MAPI:surface films showed a 68% decrease in trap density, measured by dark I-V measurements, whereas the MAPI:surface+GB films showed a 95% decrease in trap density. This was evident as a 7.5fold increase in carrier lifetime in TRPL measurements for MAPI:surface and a 10-fold increase for MAPI:surface+GB (Figure 20d). Furthermore, while MAPI:surface films showed a decrease in J-V hysteresis, MAPI:surface+GB films showed a complete disappearance of the hysteresis (Figure 20e). To

test stability, unencapsulated devices were stored at room temperature and 50% RH. After 500 hours, MAPI films fell to below 20% of initial PCE, while after 800 hours, MAPI:surface films retained 83% of initial PCE and MAPI:surface+GB films retained 95% of initial PCE (Figure 20f). Furthermore, after sitting in ambient conditions for 30 days, XRD showed a complete conversion of MAPI to PbI₂, while MAPI:surface films developed a very small PbI₂ diffraction peak and MAPI:surface+GB films showed no PbI₂ peak at all. In all, this study beautifully illustrated the importance of passivating grain boundaries in addition to surface states.

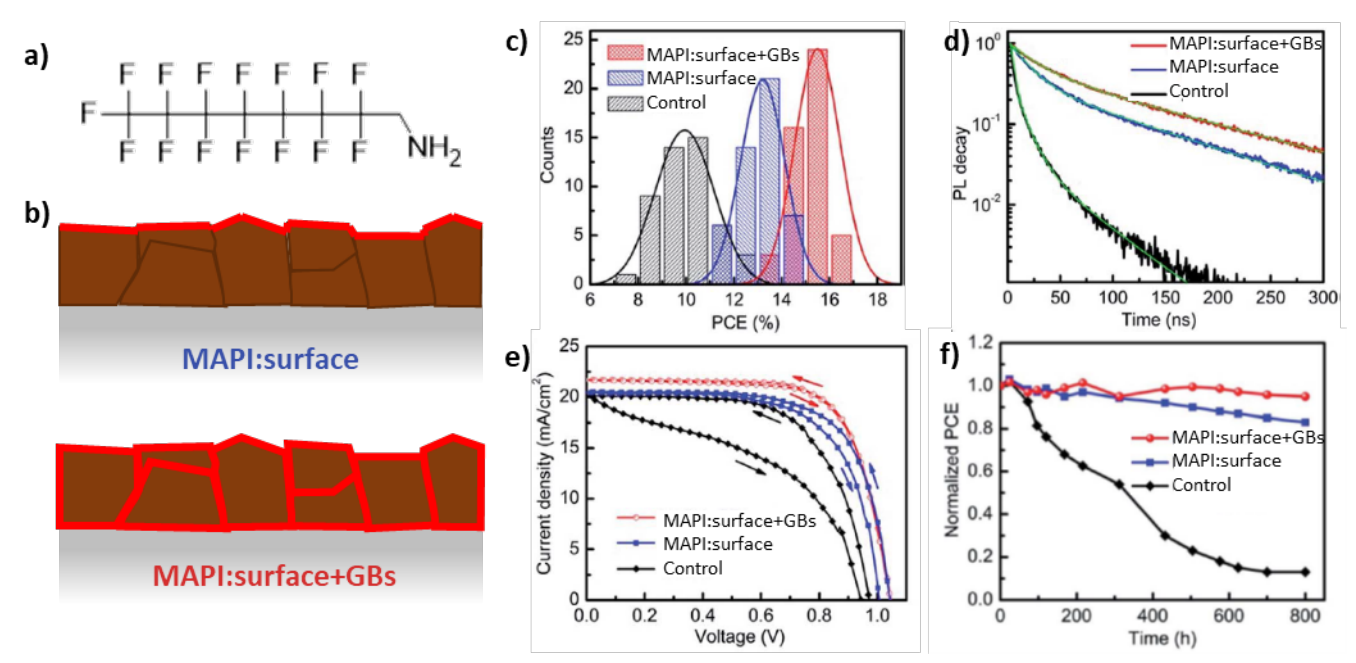


FIG. 20. a) 1*H*,1*H*-perfluorooctylamine (PFA). b) Schema for passivating the perovskite surface (top) versus surfaces and grain boundaries (bottom), where red borders indicated the PFA passivating ligand. c-f) PV performance and stability data for MAPI films (black), MAPI:surface films (blue), and MAPI:surface+GBs films (red). c) *J*-V hysteresis curves. d) TRPL decay data. e) Device PCE statistics. f) Normalized PCE versus time for unencapsulated devices stored in 50% RH air. Figures c-f adapted from reference [130], with permission. Copyright 2019, The Royal Society of Chemistry.

The studies discussed in section V so far demonstrate solution-based methods of introducing fluorocarbons. In general, solution methods require concentration optimization in order to balance the need for complete coverage with minimizing negative insulating effects such as series resistance in devices when the thicknesses of additives become too great. In addition, solution methods, as

demonstrated above, cannot always infiltrate preformed perovskite films to passivate grain boundaries in the interior of the film. One underutilized alternative route is vapor phase chemistry. Introducing passivating species in a vapor phase can possibly penetrate preformed films more effectively through Knudsen diffusion through grain boundaries. It can also support complete coverage without buildup of unnecessary material, à la self-assembled monolayers, without resolubilizing the perovskite. Zhao et al. [131] treated perovskite films with 4-fluoroaniline (FAL) vapor. The molecule and passivating technique are shown in figure 21a. FAL has a Lewis base amine group for perovskite coordination and a fluorobenzyl hydrophobic tail. Upon vapor treatment, films exhibited similar benefits to PCE and stability as other treatments presented here: 20% relative increase in PCE, 9-fold increase in carrier lifetime measured by TRPL (Figure 21b), reduced J-V hysteresis, increased PL, and improved stability against humid conditions and long-term operation. However, the new insights that the authors of this study concluded are as follows. The fluorine moiety of FAL increases the molecular dipole of the passivating ligand, which improves surface coordination as well as charge extraction at the interface. Furthermore, when compared to solution passivation using the same passivating ligand, the authors report through Kelvin probe force microscopy that the surface of vapor-treated films has a higher potential (120 mV) than solution-treated films (40 mV) (Figure 21c-e). They attributed this increased surface potential to superior alignment of ligands possible through vapor-phase chemisorption as opposed to the more randomized chemi- and physisorption of ligands from solution processing (Figure 21d,e insets). They further supported this through electrical impedance spectroscopy, showing over a 15-fold increase in recombination resistance in vapor-treated samples, which they attributed to more efficient charge separation by superior surface dipoles.

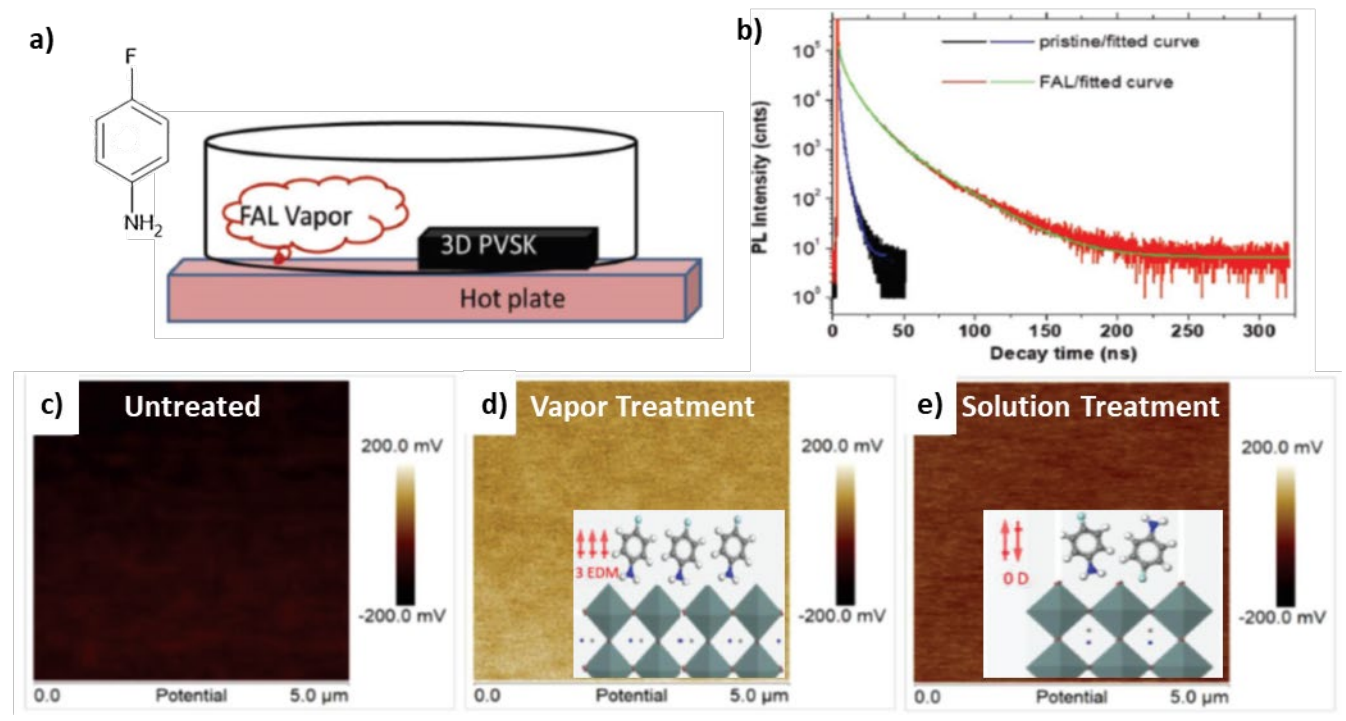


FIG. 21. a) FAL molecule and vapor passivating technique. b) TRPL of the control perovskite film (black) and the FAL-vapor-treated film (red). c-e) Kelvin probe force microscopy showing the surface potential maps of films that are untreated, treated with FAL vapor, and treated with FAL solution, respectively. Insets of (d) and (e) illustrate the proposed origin of differing surface potentials: vapor treatment more controllably applies passivating ligands in an aligned manner, allowing FAL dipole moments to align, while solution treatment results in more haphazard deposition of passivating ligands, reducing the net dipole at the perovskite surface. Figures adapted from reference [131], with permission. Copyright 2018, John Wiley and Sons.

E. Summary – fluorocarbon layers and additives

In this section, we have described various routes of incorporating fluorocarbon-based additives in perovskite solar cells as multilayers and composites and discussed the many benefits that have been seen experimentally. Improved hydrophobicity, superior layer morphology, and fluorinated surface passivation in fluorocarbon-based devices increase device longevity by impeding the infiltration of water and oxygen. Furthermore, their PV performance is enhanced through various means such as using interacting fluorocarbons to improve layer morphology and increase J_{SC} and FF, improving charge separation through permanent fluorocarbon dipoles, and tuning fluorine-dependent band alignment to increase V_{OC} . While direct fluorocarbon-perovskite interactions are experimentally indicated in a small

subset of these examples, we propose that many potential interatomic interaction modes remain unprobed, and identifying and understanding them would inform the design of more effective additives.

XI. SUMMARY AND OUTLOOK

In this Research Update, we reviewed the incorporation of fluorine and fluorocarbon moieties in perovskite halide solar cells with the goal of improving cell efficiency and stability. In *X*-site substitution with fluoride, it was reported that fluoride excludes itself from the bulk lattice and accumulates at surfaces, experimentally demonstrating trap reduction and stability enhancement through bond strengthening. Strong bonding interactions were corroborated with characterization techniques of chemical bonds such as IR spectroscopy and SS-¹H-NMR. Theoretical studies supported these bonding effects and the location of fluoride at terminal surface anion sites. When incorporated as fluorocarbon-based organic cations, fluorinated moieties served as hydrophobic spacer layers in mixed-dimensional Ruddlesden-Popper systems. They also augmented the cation dipole moments to enhance bonding effects within the materials, and improved PV performance and stability in both bulk phases and as thin surface passivators atop 3D perovskites. Finally, fluorocarbon-based hydrophobic moieties were reviewed as physiochemical encapsulation layers as well as perovskite-interacting layers and composite additives to enhance performance and stability.

In looking towards the next steps to understand and employ fluorine in halide perovskite materials, we first propose that further characterization is warranted to more fully elucidate the interatomic and intermolecular interactions at play. For instance, intermolecular interactions between various fluorinated organics and the inorganic sublattice have been presented herein to passivate surface trap states and form stable terminations at both grain boundaries and external surfaces. However, while there are a small number of published examples directly probing fluoride- and fluorocarbon-perovskite intermolecular interactions through XPS and IR spectroscopies (i.e., the Pb 4f

binding energies and the N-H stretch of the A-site organic cation), the examples are few and have yet to be extended to fluoropolymers; an atomic-scale, mechanistic understanding of such interactions is only nascent. It is quite likely that additional beneficial, intermolecular interaction modes exist for which fluorine is uniquely well suited. As previously remarked, problematic surface defects tend to include halide vacancies, and therefore surface defect passivation would include stabilization of surface iodide or replacement of surface iodide. We speculate that the class of supramolecular halogen bonds evoked in other studies [27,28] could be uniquely strong when they involve a fluorine borne by a fluorinated surface additive. Alternatively, as the C-F bond is highly polar and therefore exhibits substantial ionic character, the fluoride groups could potentially coordinate to Pb dangling bonds, exposed by iodide vacancies. In both senses, supramolecular interaction between the fluorocarbon and perovskite should alter the C-F bond character, which we propose should be detectable by peak shifts from the pristine fluorocarbon in the solid-state ¹⁹F-NMR spectrum and for the C-F stretch in the infrared (IR) spectrum. [28,54,95] IR and ¹H-NMR have been successfully used to show changes to the perovskite ammonium cation [54,95], but to our knowledge, these methods have not yet been used to assess fluorocarbon-perovskite interaction by focusing on changes in the spectroscopic observables of C-F bonding.

The significant potential for fluorine to improve perovskite stability and performance also highlights the necessity to develop synthetic approaches to more precisely incorporate fluorine at the optimal levels and locations. We propose one such approach, that, to our knowledge, has yet to be published: the thermal degradation of fluorocarbons and subsequent vapor transport of the decomposition products to produce anionic fluoride at the perovskite interface. There are examples, including our own work, in the perovskite oxide community of thermal liberation of fluoride from fluoropolymers to topochemically convert oxides to oxyfluorides at temperatures as low as 150 °C [132–137]. If topochemical fluorination can successfully fluorinate halide perovskite film surfaces, the

resultant materials would exhibit the benefits from anionic fluoride incorporation in the inorganic sublattice, as described in section III. The existence of this thermal degradation approach to fluorine incorporation also raises the interesting possibility that some adventitious decomposition of fluorinated organics may occur in many of the studies cited herein, due to the processing temperatures being as high as 180 °C. If so, perhaps some of the beneficial effects of fluorocarbons in fact stem from unintended anionic fluoride incorporation.

Though fluorocarbons have been implemented widely for their hydrophobic nature, our understanding of the bonding interactions of fluorine moieties with perovskites is in its nascence. We have strong indications of its benefits as outlined in this Research Update, and we feel that further exploration of synthetic routes to fluorine-enhanced halide perovskites could contribute substantially to this rapidly expanding field.

ACKNOWLEDGMENTS

B.M.L. and A.T.F. were supported by National Science Foundation grant CBET-1604293; S.J.M. was supported by National Science Foundation grant CMMI-1562223. We also thank Lizajane Bunyan for her comments on the manuscript.

REFERENCES

- [1] A. Kojima, K. Teshima, Y. Shirai, and T. Miyasaka, J. Am. Chem. Soc. **131**, 6050 (2009).
- [2] Natl. Renew. Energy Lab. https://www.nrel.gov/pv/cell (2020).
- [3] N. G. Park, Mater. Today **18**, 65 (2015).
- [4] W.-J. Yin, J.-H. Yang, J. Kang, Y. Yan, and S.-H. Wei, J. Mater. Chem. A Mater. Energy Sustain. **3**, 8926 (2015).
- [5] F. Zheng, L. Z. Tan, S. Liu, and A. M. Rappe, Nano Lett. **15**, 7794 (2015).
- [6] M. Petrović, V. Chellappan, and S. Ramakrishna, Sol. Energy **122**, 678 (2015).
- [7] I. L. Ivanov, A. S. Steparuk, M. S. Bolyachkina, D. S. Tsvetkov, A. P. Safronov, and A. Y. Zuev, J. Chem. Thermodyn. **116**, 253 (2018).
- [8] B. Brunetti, C. Cavallo, A. Ciccioli, G. Gigli, and A. Latini, Sci. Rep. 6, 31896 (2016).
- [9] B. Brunetti, C. Cavallo, A. Ciccioli, G. Gigli, and A. Latini, Sci. Rep. 7, 46867 (2017).
- [10] J. M. Azpiroz, E. Mosconi, J. Bisquert, and F. De Angelis, Energy Environ. Sci. 8, 2118 (2015).
- [11] C. Eames, J. M. Frost, P. R. F. Barnes, B. C. O'Regan, A. Walsh, and M. S. Islam, Nat. Commun. **6**, 7497 (2015).
- [12] J. A. Dean, in Lange's Handb. Chem., 15th ed. (McGraw-Hill, 1999).
- [13] S. Libri, N. A. Jasim, R. N. Perutz, and L. Brammer, J. Am. Chem. Soc. 130, 7842 (2008).
- [14] L. Brammer, E. A. Bruton, and P. Sherwood, New J. Chem. **23**, 965 (1999).
- [15] L. Brammer, E. A. Bruton, and P. Sherwood, Cryst. Growth Des. 1, 277 (2001).
- [16] T. Baikie, Y. Fang, J. M. Kadro, M. Schreyer, F. Wei, S. G. Mhaisalkar, M. Graetzel, and T. J. White, J. Mater. Chem. A 1, 5628 (2013).
- [17] J. Yuan, A. Hazarika, Q. Zhao, X. Ling, T. Moot, W. Ma, and J. M. Luther, Joule 4, 1160 (2020).
- [18] Q. Van Le, K. Hong, H. W. Jang, and S. Y. Kim, Adv. Electron. Mater. 4, 1800335 (2018).
- [19] Y.-H. Kim, H. Cho, and T.-W. Lee, Proc. Natl. Acad. Sci. **113**, 11694 (2016).
- [20] W.-J. Yin, T. Shi, and Y. Yan, Appl. Phys. Lett. **104**, 063903 (2014).
- [21] D. W. de Quilettes, S. M. Vorpahl, S. D. Stranks, H. Nagaoka, G. E. Eperon, M. E. Ziffer, H. J. Snaith, and D. S. Ginger, Science **348**, 683 (2015).
- [22] W. Kong, T. Ding, G. Bi, and H. Wu, Phys. Chem. Chem. Phys. 18, 12626 (2016).
- [23] H. Uratani and K. Yamashita, J. Phys. Chem. Lett. **8**, 742 (2017).
- [24] S. H. Kim and D. Lee, J. Phys. Chem. C **123**, 9629 (2019).
- [25] F. Wang, W. Geng, Y. Zhou, H.-H. Fang, C.-J. Tong, M. A. Loi, L.-M. Liu, and N. Zhao, Adv. Mater. **28**, 9986 (2016).
- [26] X. Li, M. Ibrahim Dar, C. Yi, J. Luo, M. Tschumi, S. M. Zakeeruddin, M. K. Nazeeruddin, H. Han, and M. Grätzel, Nat. Chem. **7**, 703 (2015).
- [27] A. Abate, M. Saliba, D. J. Hollman, S. D. Stranks, K. Wojciechowski, R. Avolio, G. Grancini, A. Petrozza, and H. J. Snaith, Nano Lett. **14**, 3247 (2014).
- [28] M. A. Ruiz-Preciado, D. J. Kubicki, A. Hofstetter, L. McGovern, M. H. Futscher, A. Ummadisingu, R. Gershoni-Poranne, S. M. Zakeeruddin, B. Ehrler, L. Emsley, J. V. Milić, and M. Grätzel, J. Am. Chem. Soc. **142**, 1645 (2020).
- [29] S. Yang, S. Chen, E. Mosconi, Y. Fang, X. Xiao, C. Wang, Y. Zhou, Z. Yu, J. Zhao, Y. Gao, F. De Angelis, and J. Huang, Science **365**, 473 (2019).
- [30] S. Akin, N. Arora, S. M. Zakeeruddin, M. Grätzel, R. H. Friend, and M. I. Dar, Adv. Energy Mater. **10**, 1903090 (2020).
- [31] H. Jin, E. Debroye, M. Keshavarz, I. G. Scheblykin, M. B. J. Roeffaers, J. Hofkens, and J. A. Steele, Mater. Horizons **7**, 397 (2020).

- [32] H. Zhang, M. K. Nazeeruddin, and W. C. H. Choy, Adv. Mater. 31, 1805702 (2019).
- [33] E. Smecca, Y. Numata, I. Deretzis, G. Pellegrino, S. Boninelli, T. Miyasaka, A. La Magna, and A. Alberti, Phys. Chem. Chem. Phys. **18**, 13413 (2016).
- [34] C. Müller, T. Glaser, M. Plogmeyer, M. Sendner, S. Döring, A. A. Bakulin, C. Brzuska, R. Scheer, M. S. Pshenichnikov, W. Kowalsky, A. Pucci, and R. Lovrinčić, Chem. Mater. **27**, 7835 (2015).
- [35] Y. Liu, K. Palotas, X. Yuan, T. Hou, H. Lin, Y. Li, and S.-T. Lee, ACS Nano **11**, 2060 (2017).
- [36] J. Haruyama, K. Sodeyama, L. Han, and Y. Tateyama, J. Phys. Chem. Lett. 5, 2903 (2014).
- [37] E. Mosconi, J. M. Azpiroz, and F. De Angelis, Chem. Mater. **27**, 4885 (2015).
- [38] J. M. Frost, K. T. Butler, F. Brivio, C. H. Hendon, M. van Schilfgaarde, and A. Walsh, Nano Lett. **14**, 2584 (2014).
- [39] J. A. Christians, P. A. Miranda Herrera, and P. V Kamat, J. Am. Chem. Soc. 137, 1530 (2015).
- [40] N. Aristidou, I. Sanchez-Molina, T. Chotchuangchutchaval, M. Brown, L. Martinez, T. Rath, and S. A. Haque, Angew. Chemie Int. Ed. **54**, 8208 (2015).
- [41] N. Aristidou, C. Eames, I. Sanchez-Molina, X. Bu, J. Kosco, M. S. Islam, and S. A. Haque, Nat. Commun. **8**, 15218 (2017).
- [42] A. Senocrate, T. Acartürk, G. Y. Kim, R. Merkle, U. Starke, M. Grätzel, and J. Maier, J. Mater. Chem. A 6, 10847 (2018).
- [43] L. Lanzetta, N. Aristidou, and S. A. Haque, J. Phys. Chem. Lett. 11, 574 (2020).
- [44] X.-X. Ma and Z.-S. Li, Appl. Surf. Sci. **428**, 140 (2018).
- [45] T. Leijtens, G. E. Eperon, S. Pathak, A. Abate, M. M. Lee, and H. J. Snaith, Nat. Commun. 4, 2885 (2013).
- [46] Z. Fan, H. Xiao, Y. Wang, Z. Zhao, Z. Lin, H. C. Cheng, S. J. Lee, G. Wang, Z. Feng, W. A. Goddard, Y. Huang, and X. Duan, Joule **1**, 548 (2017).
- [47] Q. Wang, B. Chen, Y. Liu, Y. Deng, Y. Bai, Q. Dong, and J. Huang, Energy Environ. Sci. **10**, 516 (2017).
- [48] R. Wang, M. Mujahid, Y. Duan, Z. Wang, J. Xue, and Y. Yang, Adv. Funct. Mater. **29**, 1808843 (2019).
- [49] A. K. Chauhan and P. Kumar, J. Phys. D. Appl. Phys. **50**, 325105 (2017).
- [50] N. H. Tiep, Z. Ku, and H. J. Fan, Adv. Energy Mater. **6**, 1501420 (2016).
- [51] X. Qin, Z. Zhao, Y. Wang, J. Wu, Q. Jiang, and J. You, J. Semicond. 38, 011002 (2017).
- [52] T. A. Berhe, W. Su, C.-H. Chen, C. Pan, J. Cheng, H.-M. Chen, M. Tsai, L. Chen, A. A. Dubale, and B. Hwang, Energy Environ. Sci. 9, 323 (2016).
- [53] D. Wang, M. Wright, N. K. Elumalai, and A. Uddin, Sol. Energy Mater. Sol. Cells 147, 255 (2016).
- [54] J. Yang, C. Liu, C. Cai, X. Hu, Z. Huang, X. Duan, X. Meng, Z. Yuan, L. Tan, and Y. Chen, Adv. Energy Mater. **9**, 1900198 (2019).
- [55] V. M. Goldschmidt, Naturwissenschaften **14**, 477 (1926).
- [56] M. Saliba, T. Matsui, K. Domanski, J.-Y. Seo, A. Ummadisingu, S. M. Zakeeruddin, J.-P. Correa-Baena, W. R. Tress, A. Abate, A. Hagfeldt, and M. Gratzel, Science **354**, 206 (2016).
- [57] D. B. Straus, S. Guo, and R. J. Cava, J. Am. Chem. Soc. **141**, 11435 (2019).
- [58] S. Dastidar, C. J. Hawley, A. D. Dillon, A. D. Gutierrez-Perez, J. E. Spanier, and A. T. Fafarman, J. Phys. Chem. Lett. **8**, 1278 (2017).
- [59] B. Li, Y. Zhang, L. Fu, T. Yu, S. Zhou, L. Zhang, and L. Yin, Nat. Commun. 9, 1076 (2018).
- [60] F. Cordero, F. Craciun, F. Trequattrini, A. Generosi, B. Paci, A. M. Paoletti, and G. Pennesi, J. Phys. Chem. Lett. **10**, 2463 (2019).
- [61] J. A. Aguiar, S. Wozny, T. G. Holesinger, T. Aoki, M. K. Patel, M. Yang, J. J. Berry, M. Al-Jassim, W. Zhou, and K. Zhu, Energy Environ. Sci. **9**, 2372 (2016).
- [62] J. S. Yun, J. Kim, T. Young, R. J. Patterson, D. Kim, J. Seidel, S. Lim, M. A. Green, S. Huang, and A. Ho-Baillie, Adv. Funct. Mater. **28**, 1705363 (2018).

- [63] I. Chung, J.-H. Song, J. Im, J. Androulakis, C. D. Malliakas, H. Li, A. J. Freeman, J. T. Kenney, and M. G. Kanatzidis, J. Am. Chem. Soc. **134**, 8579 (2012).
- [64] P. Xu, S. Chen, H.-J. Xiang, X.-G. Gong, and S.-H. Wei, Chem. Mater. **26**, 6068 (2014).
- [65] K. P. Marshall, R. I. Walton, and R. A. Hatton, J. Mater. Chem. A 3, 11631 (2015).
- [66] T. Leijtens, R. Prasanna, A. Gold-Parker, M. F. Toney, and M. D. McGehee, ACS Energy Lett. **2**, 2159 (2017).
- [67] R. Nishikubo, N. Ishida, Y. Katsuki, A. Wakamiya, and A. Saeki, J. Phys. Chem. C 121, 19650 (2017).
- [68] M. Konstantakou and T. Stergiopoulos, J. Mater. Chem. A 5, 11518 (2017).
- [69] R. J. Stewart, C. Grieco, A. V Larsen, J. J. Maier, and J. B. Asbury, J. Phys. Chem. Lett. **7**, 1148 (2016).
- [70] X. Zheng, Y. Hou, C. Bao, J. Yin, F. Yuan, Z. Huang, K. Song, J. Liu, J. Troughton, N. Gasparini, C. Zhou, Y. Lin, D.-J. Xue, B. Chen, A. K. Johnston, N. Wei, M. N. Hedhili, M. Wei, A. Y. Alsalloum, P. Maity, B. Turedi, C. Yang, D. Baran, T. D. Anthopoulos, Y. Han, Z.-H. Lu, O. F. Mohammed, F. Gao, E. H. Sargent, and O. M. Bakr, Nat. Energy **5**, 131 (2020).
- [71] Z. Yang, J. Dou, S. Kou, J. Dang, Y. Ji, G. Yang, W. Wu, D. Kuang, and M. Wang, Adv. Funct. Mater. **30**, 1910710 (2020).
- [72] J. H. Noh, S. H. Im, J. H. Heo, T. N. Mandal, and S. Il Seok, Nano Lett. 13, 1764 (2013).
- [73] R. K. Misra, S. Aharon, B. Li, D. Mogilyansky, I. Visoly-Fisher, L. Etgar, and E. A. Katz, J. Phys. Chem. Lett. 6, 326 (2015).
- [74] E. T. Hoke, D. J. Slotcavage, E. R. Dohner, A. R. Bowring, H. I. Karunadasa, and M. D. McGehee, Chem. Sci. 6, 613 (2015).
- [75] C. G. Bischak, C. L. Hetherington, H. Wu, S. Aloni, D. F. Ogletree, D. T. Limmer, and N. S. Ginsberg, Nano Lett. 17, 1028 (2017).
- [76] Q. Chen, H. Zhou, Y. Fang, A. Z. Stieg, T.-B. Song, H.-H. Wang, X. Xu, Y. Liu, S. Lu, J. You, P. Sun, J. McKay, M. S. Goorsky, and Y. Yang, Nat. Commun. **6**, 7269 (2015).
- [77] S. Dastidar, D. A. Egger, L. Z. Tan, S. B. Cromer, A. D. Dillon, S. Liu, L. Kronik, A. M. Rappe, and A. T. Fafarman, Nano Lett. **16**, 3563 (2016).
- [78] R. D. Shannon, Acta Crystallogr. Sect. A **32**, 751 (1976).
- [79] L. Fan, Y. Ding, J. Luo, B. Shi, X. Yao, C. Wei, D. Zhang, G. Wang, Y. Sheng, Y. Chen, A. Hagfeldt, Y. Zhao, and X. Zhang, J. Mater. Chem. A 5, 7423 (2017).
- [80] M. Kim, G.-H. Kim, T. K. Lee, I. W. Choi, H. W. Choi, Y. Jo, Y. J. Yoon, J. W. Kim, J. Lee, D. Huh, H. Lee, S. K. Kwak, J. Y. Kim, and D. S. Kim, Joule **3**, 2179 (2019).
- [81] Q. Wang, M. Lyu, M. Zhang, J. H. Yun, H. Chen, and L. Wang, J. Phys. Chem. Lett. 6, 4379 (2015).
- [82] I. Chung, B. Lee, J. He, R. P. H. Chang, and M. G. Kanatzidis, Nature 485, 486 (2012).
- [83] G. Xing, M. H. Kumar, W. K. Chong, X. Liu, Y. Cai, H. Ding, M. Asta, M. Grätzel, S. Mhaisalkar, N. Mathews, and T. C. Sum, Adv. Mater. **28**, 8191 (2016).
- [84] S. Gupta and G. Hodes, SN Appl. Sci. **1**, 1066 (2019).
- [85] M. H. Kumar, S. Dharani, W. L. Leong, P. P. Boix, R. R. Prabhakar, T. Baikie, C. Shi, H. Ding, R. Ramesh, M. Asta, M. Graetzel, S. G. Mhaisalkar, and N. Mathews, Adv. Mater. **26**, 7122 (2014).
- [86] W. Liao, D. Zhao, Y. Yu, C. R. Grice, C. Wang, A. J. Cimaroli, P. Schulz, W. Meng, K. Zhu, R.-G. Xiong, and Y. Yan, Adv. Mater. **28**, 9333 (2016).
- [87] M. Xiao, S. Gu, P. Zhu, M. Tang, W. Zhu, R. Lin, C. Chen, W. Xu, T. Yu, and J. Zhu, Adv. Opt. Mater.6, 1700615 (2018).
- [88] E. L. Unger, A. R. Bowring, C. J. Tassone, V. L. Pool, A. Gold-Parker, R. Cheacharoen, K. H. Stone, E. T. Hoke, M. F. Toney, and M. D. McGehee, Chem. Mater. **26**, 7158 (2014).
- [89] S. Colella, E. Mosconi, G. Pellegrino, A. Alberti, V. L. P. Guerra, S. Masi, A. Listorti, A. Rizzo, G. G. Condorelli, F. De Angelis, and G. Gigli, J. Phys. Chem. Lett. **5**, 3532 (2014).
- [90] K. P. Marshall, M. Walker, R. I. Walton, and R. A. Hatton, Nat. Energy 1, 16178 (2016).

- [91] X. Liu, Y. Wang, T. Wu, X. He, X. Meng, J. Barbaud, H. Chen, H. Segawa, X. Yang, and L. Han, Nat. Commun. **11**, 2678 (2020).
- [92] J. Wu, F. Fang, Z. Zhao, T. Li, R. Ullah, Z. Lv, Y. Zhou, and D. Sawtell, RSC Adv. 9, 37119 (2019).
- [93] Z. Zhao, J. Wu, F. Fang, T. Li, Y. Zhou, and J. Wang, Mater. Res. Express **6**, 125534 (2019).
- [94] S. J. Lee, S. S. Shin, Y. C. Kim, D. Kim, T. K. Ahn, J. H. Noh, J. Seo, and S. Il Seok, J. Am. Chem. Soc. **138**, 3974 (2016).
- [95] N. Li, S. Tao, Y. Chen, X. Niu, C. K. Onwudinanti, C. Hu, Z. Qiu, Z. Xu, G. Zheng, L. Wang, Y. Zhang, L. Li, H. Liu, Y. Lun, J. Hong, X. Wang, Y. Liu, H. Xie, Y. Gao, Y. Bai, S. Yang, G. Brocks, Q. Chen, and H. Zhou, Nat. Energy 4, 408 (2019).
- [96] D.-Y. Son, S.-G. Kim, J.-Y. Seo, S.-H. Lee, H. Shin, D. Lee, and N.-G. Park, J. Am. Chem. Soc. **140**, 1358 (2018).
- [97] X. Yi, Z. Zhang, A. Chang, Y. Mao, Y. Luan, T. Lin, Y. Wei, Y. Zhang, F. Wang, S. Cao, C. Li, and J. Wang, Adv. Energy Mater. **9**, 1901726 (2019).
- [98] Q. Li, Y. Zhao, R. Fu, W. Zhou, Y. Zhao, X. Liu, D. Yu, and Q. Zhao, Adv. Mater. **30**, 1803095 (2018).
- [99] Y. Zhao, H. Tan, H. Yuan, Z. Yang, J. Z. Fan, J. Kim, O. Voznyy, X. Gong, L. N. Quan, C. S. Tan, J. Hofkens, D. Yu, Q. Zhao, and E. H. Sargent, Nat. Commun. **9**, 1607 (2018).
- [100] C. Wu, K. Wang, X. Feng, Y. Jiang, D. Yang, Y. Hou, Y. Yan, M. Sanghadasa, and S. Priya, Nano Lett. **19**, 1251 (2019).
- [101] L. Fu, Y. Zhang, B. Chang, B. Li, S. Zhou, L. Zhang, and L. Yin, J. Mater. Chem. A 6, 13263 (2018).
- [102] G. Grancini and M. K. Nazeeruddin, Nat. Rev. Mater. 4, 4 (2019).
- [103] A. Shokri, X.-B. Wang, and S. R. Kass, J. Am. Chem. Soc. **135**, 9525 (2013).
- [104] F. El-Mellouhi, S. N. Rashkeev, A. Marzouk, L. Kabalan, A. Belaidi, B. Merzougui, N. Tabet, and F. H. Alharbi, J. Mater. Chem. C **7**, 5299 (2019).
- [105] F. Zhang, D. H. Kim, H. Lu, J.-S. Park, B. W. Larson, J. Hu, L. Gao, C. Xiao, O. G. Reid, X. Chen, Q. Zhao, P. F. Ndione, J. J. Berry, W. You, A. Walsh, M. C. Beard, and K. Zhu, J. Am. Chem. Soc. 141, 5972 (2019).
- [106] J. Shi, Y. Gao, X. Gao, Y. Zhang, J. Zhang, X. Jing, and M. Shao, Adv. Mater. **31**, 1901673 (2019).
- [107] G. Liu, X.-X. Xu, S. Xu, L. Zhang, H. Xu, L. Zhu, X. Zhang, H. Zheng, and X. Pan, J. Mater. Chem. A **8**, 5900 (2020).
- [108] Y. Liu, S. Akin, L. Pan, R. Uchida, N. Arora, J. V. Milić, A. Hinderhofer, F. Schreiber, A. R. Uhl, S. M. Zakeeruddin, A. Hagfeldt, M. I. Dar, and M. Grätzel, Sci. Adv. **5**, eaaw2543 (2019).
- [109] J. S. Yun, J. Seidel, J. Kim, A. M. Soufiani, S. Huang, J. Lau, N. J. Jeon, S. Il Seok, M. A. Green, and A. Ho-Baillie, Adv. Energy Mater. **6**, 1600330 (2016).
- [110] R. Ishikawa, K. Ueno, and H. Shirai, Org. Electron. **78**, 105596 (2020).
- [111] H. Xu, Y. Sun, H. Zheng, G. Liu, X. Xu, S. Xu, L. Zhang, X. Chen, and X. Pan, J. Mater. Chem. C **7**, 15276 (2019).
- [112] S. Zhao, B. Zhao, Y. Chen, G. Yang, and X. Li, ACS Appl. Energy Mater. 2, 6230 (2019).
- [113] I. Hwang, I. Jeong, J. Lee, M. J. Ko, and K. Yong, ACS Appl. Mater. Interfaces 7, 17330 (2015).
- [114] F. Bella, G. Griffini, J.-P. Correa-Baena, G. Saracco, M. Gratzel, A. Hagfeldt, S. Turri, and C. Gerbaldi, Science **354**, 203 (2016).
- [115] G.-H. Kim, H. Jang, Y. J. Yoon, J. Jeong, S. Y. Park, B. Walker, I.-Y. Jeon, Y. Jo, H. Yoon, M. Kim, J.-B. Baek, D. S. Kim, and J. Y. Kim, Nano Lett. **17**, 6385 (2017).
- [116] H. Liu, M. Wang, J. Bian, Y. Feng, Z. Wang, B. Zhang, and Y. Shi, Appl. Phys. Lett. **113**, 023902 (2018).
- [117] L. Lei, S. Yang, Y. Yu, M. Li, J. Xie, S. Bao, P. Jin, and A. Huang, J. Mater. Chem. A 7, 21085 (2019).
- [118] Z. Hawash, L. K. Ono, S. R. Raga, M. V. Lee, and Y. Qi, Chem. Mater. 27, 562 (2015).
- [119] M. Stolterfoht, P. Caprioglio, C. M. Wolff, J. A. Márquez, J. Nordmann, S. Zhang, D. Rothhardt, U. Hörmann, Y. Amir, A. Redinger, L. Kegelmann, F. Zu, S. Albrecht, N. Koch, T. Kirchartz, M. Saliba,

- T. Unold, and D. Neher, Energy Environ. Sci. **12**, 2778 (2019).
- [120] I. Jeong, J. W. Jo, S. Bae, H. J. Son, and M. J. Ko, Dye. Pigment. 164, 1 (2019).
- [121] Y. Kim, E. H. Jung, G. Kim, D. Kim, B. J. Kim, and J. Seo, Adv. Energy Mater. 8, 1801668 (2018).
- [122] R. Azmi, U.-H. Lee, F. T. A. Wibowo, S. H. Eom, S. C. Yoon, S.-Y. Jang, and I. H. Jung, ACS Appl. Mater. Interfaces 10, 35404 (2018).
- [123] J. W. Jo, J. W. Jung, H.-W. Wang, P. Kim, T. P. Russell, and W. H. Jo, Chem. Mater. 26, 4214 (2014).
- [124] M. Jeong, I. W. Choi, E. M. Go, Y. Cho, M. Kim, B. Lee, S. Jeong, Y. Jo, H. W. Choi, J. Lee, J. Bae, S. K. Kwak, D. S. Kim, and C. Yang, Science 369, 1615 (2020).
- [125] S. Valero, T. Soria, N. Marinova, and J. L. Delgado, Polym. Chem. 10, 5726 (2019).
- [126] S. Zhang, Y. Lu, B. Lin, Y. Zhu, K. Zhang, N.-Y. Yuan, J.-N. Ding, and B. Fang, Sol. Energy Mater. Sol. Cells **170**, 178 (2017).
- [127] Y. Rong, S. Venkatesan, R. Guo, Y. Wang, J. Bao, W. Li, Z. Fan, and Y. Yao, Nanoscale **8**, 12892 (2016).
- [128] Y. Moriya, R. Ishikawa, S. Akiyama, K. Ueno, and H. Shirai, Chem. Lett. 49, 87 (2020).
- [129] E. Jia, D. Wei, P. Cui, J. Ji, H. Huang, H. Jiang, S. Dou, M. Li, C. Zhou, and W. Wang, Adv. Sci. **6**, 1900252 (2019).
- [130] P. Guo, Q. Ye, X. Yang, J. Zhang, F. Xu, D. Shchukin, B. Wei, and H. Wang, J. Mater. Chem. A **7**, 2497 (2019).
- [131] S. Zhao, J. Xie, G. Cheng, Y. Xiang, H. Zhu, W. Guo, H. Wang, M. Qin, X. Lu, J. Qu, J. Wang, J. Xu, and K. Yan, Small **14**, 1803350 (2018).
- [132] T. Katayama, A. Chikamatsu, Y. Hirose, R. Takagi, H. Kamisaka, T. Fukumura, and T. Hasegawa, J. Mater. Chem. C 2, 5350 (2014).
- [133] E. J. Moon, Y. Xie, E. D. Laird, D. J. Keavney, C. Y. Li, and S. J. May, J. Am. Chem. Soc. **136**, 2224 (2014).
- [134] A. Chikamatsu, T. Maruyama, T. Katayama, Y. Su, Y. Tsujimoto, K. Yamaura, M. Kitamura, K. Horiba, H. Kumigashira, and T. Hasegawa, Phys. Rev. Mater. **4**, 025004 (2020).
- [135] J. Wang, Y. Shin, E. Arenholz, B. M. Lefler, J. M. Rondinelli, and S. J. May, Phys. Rev. Mater. **2**, 073407 (2018).
- [136] B. M. Lefler, T. Duchoň, G. Karapetrov, J. Wang, C. M. Schneider, and S. J. May, Phys. Rev. Mater. **3**, 073802 (2019).
- [137] O. Clemens, F. J. Berry, A. J. Wright, K. S. Knight, J. M. Perez-Mato, J. M. Igartua, and P. R. Slater, J. Solid State Chem. **206**, 158 (2013).